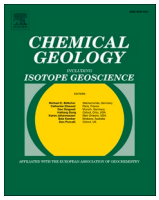
Chemical Geology 704 (2026) 123266



Contents lists available at ScienceDirect

Chemical Geology

journal homepage: www.elsevier.com/locate/chemgeo



Hydrogen generation potential of peridotites and pyroxenites in ophiolitic settings

Vivian Azor de Freitas [a,b], Tiziano Boschetti [a], Isabelle Moretti [c], Alessandra Montanini [a,*]

[a] Department of Chemistry, Life Science and Environmental Sustainability, University of Parma, Parco Area delle Scienze,157/a, 43124 Parma, Italy
[b] National Agency of Petroleum, Natural Gas and Biofuels (ANP), Avenida Rio Branco 65, 20090-004 Rio de Janeiro, Brazil
[c] Université de Pau et des Pays de l'Adour, E2S UPPA, LFCR, Pau, France

ARTICLE INFO

Editor: Marco Fiorentini

Keywords:
Natural hydrogen
Ultramafic rocks
Ophiolites
Serpentinization
Fluid-rock interactions
Northern Apennines
Mt. Prinzera

ABSTRACT

The partially serpentinized mantle bodies exposed in the western sector of the Northern Apennines, Italy, represent a favorable environment for natural hydrogen (H_2) studies, particularly Mt. Prinzera, which hosts a hyperalkaline spring containing dissolved H_2. A geochemical characterization of peridotite, pyroxenite, and serpentinite samples was carried out to reconstruct the past and present stages of serpentinization and to assess their H_2 generation potential. This study combined mineralogical, whole-rock compositional, and redox-state analyses, along with thermodynamic modeling of spring waters. The major serpentinization event associated with mantle exhumation in the Middle to Late Jurassic was marked by extensive replacement of olivine, clinopyroxene, orthopyroxene by serpentine and subordinate magnetite. Alteration was more intense in olivine than in pyroxenes, resulting in higher serpentinization degrees in peridotites (~ 50 vol%), compared to pyroxenites (~ 10 vol%). Mineralogical evidence suggests temperatures of approximately 220 °C and 300 °C for this stage. Currently, serpentinization and H_2 generation are likely active at Mt. Prinzera, with fluid-rock interactions involving particularly the oxidation of a small fraction of Fe^{2+}-serpentine and/or magnetite, rather than the primary mineral assemblage. Thermodynamic equilibria, based on the activities obtained from the aqueous speciation, and the isotope composition of the hyperalkaline water were used to estimate the temperature at depth, which appears to be markedly low. Thus, serpentinization may occur either at the base of Mt. Prinzera or within a deeper, hidden ultramafic body. In addition, trapped H_2 accumulations originating from earlier serpentinization stages can also be considered.

1. Introduction

Dihydrogen (H_2), the most abundant molecule in the universe and a key molecule for understanding the origin of life (Russell et al., 2010), is rare in the Earth's atmosphere, occurring at concentrations below one ppm (Lide, 2004). As a result, hydrogen has been produced industrially for decades, primarily using steam methane reforming and coal gasification, mainly to supply the chemical industry, oil refining, and steel production. More recently, interest in low-emission hydrogen has grown, driven by global efforts to achieve Net Zero Emissions by 2050 (IEA, 2024). In the context of low-emission energy, natural or native (H_2) – generated by natural subsurface processes without industrial intervention – may contribute to reduced net emissions.

Several processes can generate natural H_2 in geological environments, including oxidation of iron-rich rocks via water-rock reactions, radiolysis of water caused by radioactive elements present in crustal rocks, and thermal maturation of organic matter (Klein et al., 2020; Lévy et al., 2023). Other secondary mechanisms can produce hydrogen, including mechanoradical reactions along faults (Lefeuvre et al., 2025) or biological activity (Zgonnik, 2020).

The oxidation of ferrous Fe (Fe^{2+}) to ferric Fe (Fe^{3+}), which occurs in natural processes such as the serpentinization of ultramafic rocks, is one of the key mechanisms for natural H_2 generation (Worman et al., 2020). In particular, during the serpentinization of olivine, Fe^{2+} originally present in the minerals reacts with water and is oxidized to Fe^{3+}. This process primarily leads to the formation of serpentine-group minerals (e.g., lizardite, chrysotile, antigorite), along with varying amounts of brucite and magnetite, and generates H_2 (McCollom et al., 2022, Eq.

* Corresponding author at: Department of Chemistry, Life Science and Environmental Sustainability, University of Parma, Parco Area delle Scienze,157/a, 43100 Parma, Italy.
E-mail address: alessandra.montanini@unipr.it (A. Montanini).

https://doi.org/10.1016/j.chemgeo.2026.123266
Received 17 September 2025; Received in revised form 7 January 2026; Accepted 21 January 2026
Available online 25 January 2026
0009-2541/© 2026 The Authors. Published by Elsevier B.V. This is an open access article under the CC BY-NC-ND license (http://creativecommons.org/licenses/by-nc-nd/4.0/).

(1)).

$$\underset{\text{olivine}}{(MgFe)_2SiO_4} + vH_2O \rightarrow w\underset{\text{serpentine}}{(Mg, Fe^{2+}, Fe^{3+})_3(SiFe^{3+})_2O_5(OH)_4} \pm x\underset{\text{brucite}}{(MgFe^{2+})(OH)_2} \pm y\underset{\text{magnetite}}{Fe^{2+}Fe_2{}^{3+}O_4} + z\mathbf{H_2} \quad (1)$$

where, the coefficients v-z represent the stoichiometric parameters of the reaction. The serpentinization of pyroxene also produces H_2, although likely at lower quantities compared to olivine and at higher temperatures (Klein et al., 2013). In addition to serpentine and magnetite, this process can generate relatively high amounts of talc and tremolite, releasing SiO_2 and Ca into the system (Macleod et al., 1994; Allen and Seyfried Jr, 2003; Klein et al., 2013) as illustrated by the simplified reaction shown in Eq. (2), based on Macleod et al. (1994).

$$\text{pyroxene} + H_2O \rightarrow \text{serpentine} + SiO_2 + \text{magnetite} + Ca^{2+} + OH^- + \mathbf{H_2} \quad (2)$$

Other secondary minerals, such as Ni—Fe alloys and chlorite, may form during the serpentinization of olivine and pyroxene process, depending on pressure and temperature conditions (Holm et al., 2015).

Additionally, the release of OH^- ions during the serpentinization process increases the pH of the associated fluids, often exceeding 9. Therefore, the generation of H_2 in ultramafic geological contexts is often, but not always, associated with hyperalkaline waters (Holm et al., 2015, and references therein).

Ophiolite complexes, characterized by high content of iron-bearing rocks, provide favorable conditions for serpentinization and H_2 production. Globally, various studies have investigated H_2 occurrence linked to ophiolitic settings (e.g., Vacquand et al., 2018; Zgonnik et al., 2019; Lefeuvre et al., 2021; Etiope, 2023; Loiseau et al., 2024; Pasquet et al., 2025). In Italy, although research specifically targeting this topic remains limited, a few studies have addressed it, such as Leila et al. (2021) in the Larderello geothermal field and Dugamin et al. (2019) on the Lanzo Peridotite in the Alps. Other studies not directly focused on H_2 have nonetheless reported variable H_2 concentrations in ophiolitic contexts in Italy (Duchi et al., 2005; Boschetti et al., 2013; Boulart et al., 2013; Etiope and Whiticar, 2019).

The occurrence of hyperalkaline springs associated with ophiolitic rocks in the western part of the Northern Apennines has motivated previous investigations into the presence of natural H_2 in this continental ophiolitic setting (Boschetti et al., 2013; Freitas et al., 2025). This study targeted various locations, primarily focusing on outcrops of External and Internal Ligurian ophiolites and their surroundings areas. Dissolved H_2 was detected in various springs across the investigated areas, among which the Mt. Prinzera ultramafic body was selected for a more detailed study. Located approximately 25 km southwest of Parma, Mt. Prinzera predominantly consists of peridotites and pyroxenites exhibiting varying degrees of serpentinization, a process likely to be closely correlated with H_2 generation in the area.

This study focuses on characterizing the natural hydrogen (H_2) generation potential of the ultramafic rocks at Mt. Prinzera. To achieve this, a multi-technique analytical approach was applied to a set of representative rock samples, covering the main lithological types found in the area. These include bulk-rock geochemical analyses and detailed mineralogical investigations carried out through petrography studies, electron probe microanalysis, and Mössbauer spectroscopy. Peridotites emerged as the most promising rock type for H_2 generation, due to their high olivine content and the well-established link between olivine serpentinization and H_2 production. Pyroxenites were also examined, as they host iron-bearing minerals that may play a role in H_2 production. In addition, serpentinites were analyzed to reconstruct the history of serpentinization and to assess its implications for past H_2 generation processes.

2. Geological background and the study area description

The ophiolitic rocks exposed in the western sector of the Northern Apennines fold-and-thrust belt are remnants of the oceanic lithosphere that formed during the opening and subsequent closure of the northern branch of the Western Tethys, known as the Ligure-Piemontese basin. The geological evolution of this basin – from its formation during Mesozoic extensional events, to its closure under compressional tectonics from Late Cretaceous to the Early Oligocene – is recorded in the Ligurian Units (Marroni et al., 2017; Conti et al., 2020). These units include both oceanic lithosphere and associated sedimentary sequences and they are divided into Internal and External Ligurian domains, which correspond to the distal and proximal domains of the former Ligure-Piemontese oceanic basin, respectively (Sanfilippo and Tribuzio, 2011).

The Internal Ligurian ophiolites are characterized by the absence of continental material and consist of a basement composed of gabbroic intrusions emplaced within mantle peridotites, overlain by volcano-sedimentary cover sequences (Tribuzio et al., 1997).

The External Ligurian ophiolites represent mantle material uplifted onto the ocean floor during the oceanic spreading. The ophiolites occur as slide blocks of mantle-derived ultramafic rocks, MOR-type basalts, and minor gabbros, enclosed within sedimentary mélanges (Marroni et al., 1998; Montanini et al., 2008).

Mantle-derived bodies in the External Ligurian ophiolites, extending over several kilometers, are primarily composed of spinel-plagioclase lherzolites, often interlayered with thin pyroxenite layers (Montanini et al., 2006; Ferrari et al., 2022). Mt. Prinzera, located in the Taro Valley (Parma Province), represents one of these bodies (Fig. 1). It forms an elongated NE-SW-aligned massif extending for 1.7 km in length, reaching 736 m in elevation, with a vertical difference of about 200 m from its base to the summit. The outcrops mainly consist of spinel-bearing peridotites displaying porphyroclastic textures, with olivine, clinopyroxene, and orthopyroxene porphyroclasts reaching up to 1 cm in size. Serpentinization is pervasive throughout the peridotites, in some cases leading to complete transformation into serpentinite, while better preservation is observed in the associated pyroxenites.

Previous studies measured dissolved H_2 in spring waters at two locations in the western part of Mt. Prinzera: one in a hyperalkaline spring (pH 11.2, H_2: 0.28–0.79 μM) near its base, and another in a slightly alkaline spring (pH 7.7, H_2: 0.44 μM) located a few hundred meters to the southwest (Fig. 1; Boschetti et al., 2013; Freitas et al., 2025). The H_2 concentration at Mt. Prinzera, compared with that of other hyperalkaline springs worldwide, is considered low, as shown in Fig. 4 of Freitas et al. (2025). No dissolved H_2 was detected (detection limit: 5 ppmv) in the near-neutral springs (pH ~ 7.5) from the eastern and southern sectors of Mt. Prinzera (Freitas et al., 2025).

3. Material and methods

For this study, 14 samples of ultramafic lithologies from Mt. Prinzera were selected. Four of these samples (AM-288b, AM-371, AM-403, and AM-483) were already included in datasets used in previous petrogenetic studies (Montanini et al., 2006; Montanini and Tribuzio, 2015). Six samples (VAF-4 A, VAF—4B, VAF-5, VAF-6, VAF-7 A, and VAF-8) were collected in May 2024, whereas samples AM-332, AM-372, AM-394, and AM-419 were obtained from available dataset. All these samples were added to the dataset to enhance the representativeness and spatial coverage of the Mt. Prinzera sample suite. Petrographic and whole-rock chemical analyses were carried out on all samples, while selected subsets were analyzed using Electron Probe Microanalyzer (EPMA), Electron Microprobe with energy Dispersive Microanalytic System (SEM-EDS), and Mössbauer spectroscopy, as detailed in the following sections.

3.1. Petrographic study

The thin sections were examined under transmitted and reflected

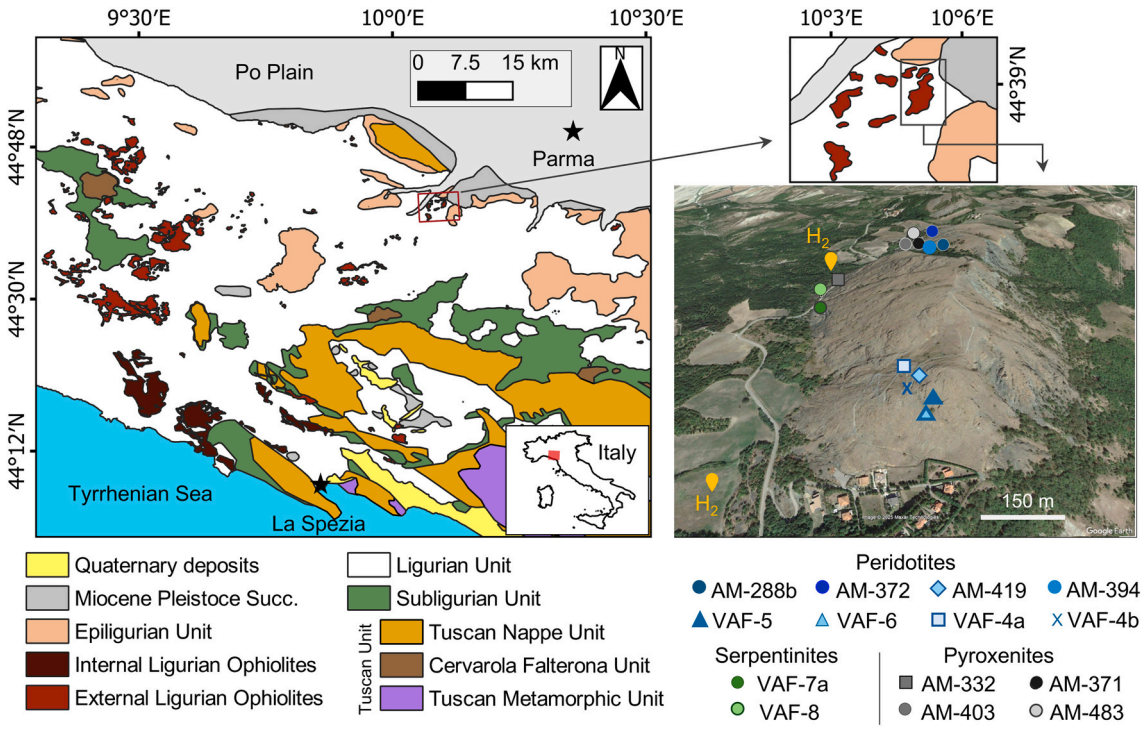


Fig. 1. Regional geological map of the Northern Apennines (Italy) displaying the location of Mt. Prinzera and the sampling points, categorized by lithotype. The geological units and ophiolite bodies are based on the Geological Map of Northern Apennines (Conti et al., 2020). Satellite image from Google Earth Pro 2025, satellite image date 9/9/2024.

light using a Leitz optical microscope. The focus was on identifying the minerals involved in the serpentinization process and describing their textural relationships (Supplementary Material 1, Document A). Based on this analysis, the modal proportions of primary minerals (Supplementary Data, Table A) and the degree of serpentinization were estimated, and accessory minerals associated with this process were recognized.

3.2. Mineral analyses using EPMA and SEM-EDS

Five samples with variable degrees of serpentinization (VAF-4 A, VAF-5, VAF-6, VAF-7 A, and AM-332, Supplementary Data, Table B) were analyzed at the EPMA (Electron Probe Microanalyzer) facility of the Unitech COSPECT (University of Milan, Italy) using a JEOL JXA-8200 Super Probe. An accelerating voltage of 15 kV was applied for all analyses. All minerals were measured using a beam current of 15 nA and a beam size of 1 μm. The counting time was 30 s for the peak and 10 s for the background. Backscattered electron (BSE) images were obtained in some areas to distinguish iron-rich phases. Analyses of samples AM-288b, AM-371, AM-372, and AM-419 were performed at the University of Parma (Italy) facility using a JEOL 6400 SEM equipped with an Oxford-ISIS EDS. Operating conditions were an accelerating voltage of 15 kV, a beam current of 0.25 nA, and natural minerals and synthetic compounds were used as standards.

Analyses were performed on porphyroclasts (when present) and matrix crystals of olivine (Ol), orthopyroxene (Opx), clinopyroxene (Cpx), serpentine (Srp), spinel (Spl), amphibole (Amp), magnetite (Mag), and fine-grained matrix phases not previously identified during the petrographic studies.

3.3. Bulk-rock compositional analyses

Whole-rock analysis of major oxides was carried out at Activation Labs (Ontario, Canada) on 10 samples (VAF-4a, VAF-4b, VAF-5, VAF-6, VAF-7a, VAF-8, AM-332, AM-372, AM-394, and AM-419) using Inductively Coupled Plasma Optical Emission Spectroscopy (ICP-OES) with an accuracy of 1%. These new data, together with previously published whole-rock chemical data for samples AM-288b, AM-371, AM-403, and AM-483 (Montanini et al., 2012.; Montanini and Tribuzio, 2015), were integrated with Fe speciation data obtained at Activation Labs by titration following cold acid digestion of ammonium metavanadate, and hydrofluoric acid in an open system (accuracy of 2.1% and precision of 2.5%). The major oxide contents, reported in Table C of the Supplementary Data, were normalized on an anhydrous basis.

3.4. Mössbauer spectroscopy

Mössbauer analyses were performed on powdered bulk rocks from three samples (VAF-4 A, AM-371, and AM-394) at the Charles Gerhardt Institute of the University of Montpellier (France). Acquisition of ^{57}Fe Mössbauer spectra was conducted in transmission mode using a constant acceleration spectrometer equipped with a ^{57}Co/Rh source. Measurements were carried out at low velocity (from −4 to 4 mm/s) and room temperature (295 K) in a zero magnetic field. The hyperfine parameters were fitted using the Liouville operator based on the Fullham program. This approach enabled the determination of the individual subspectral parameters (isomer shift, quadrupole splitting) and the relative areas of the various Fe contributions (Sougrati et al., 2008, 2016). Petrographic and compositional analyses previously performed on the samples, along with theoretical hyperfine parameters of the minerals, available in the literature (Geymond et al., 2025 and references therein), were essential for guiding the correlation between the fitted spectra and the most appropriate minerals, as well as their iron speciation.

3.5. Hydrogeochemical speciation and thermodynamic calculations

For the hydrogeochemical speciation and thermodynamic calculations, the average chemical and physicochemical composition of the hyperalkaline spring at Mt. Prinzera was considered, based on samples collected between 1998 and 2023 (Boschetti and Toscani, 2008;

Boschetti et al., 2013; Segadelli et al., 2017; Freitas et al., 2025; Supplementary Data, Table D).

The calculation of the activity of dissolved constituents, gases fugacities, minerals-water saturation indices, and construction of activity diagrams were carried out using the software suite The Geochemist's Workbench, version 18 (GWB; Bethke et al., 2025).

The thermodynamic database used for the above calculations was generated with PyGeochemCalc, version 1.4.0 (PyGCC), using the speq21.dat database (Awolayo and Tutolo, 2022). In this database, most of the fundamental thermodynamic parameters for serpentine phases such as lizardite, hisingerite, cronstedtite, Mg-cronstedtite, and greenalite are from Tutolo et al. (2020), except Fe^{2+}-serpentine (a lizardite0.9-greenalite0.1 solid solution) and amorphous magnetite, i.e., magnetite(am). For Fe^{2+}-serpentine, both the basic thermodynamic

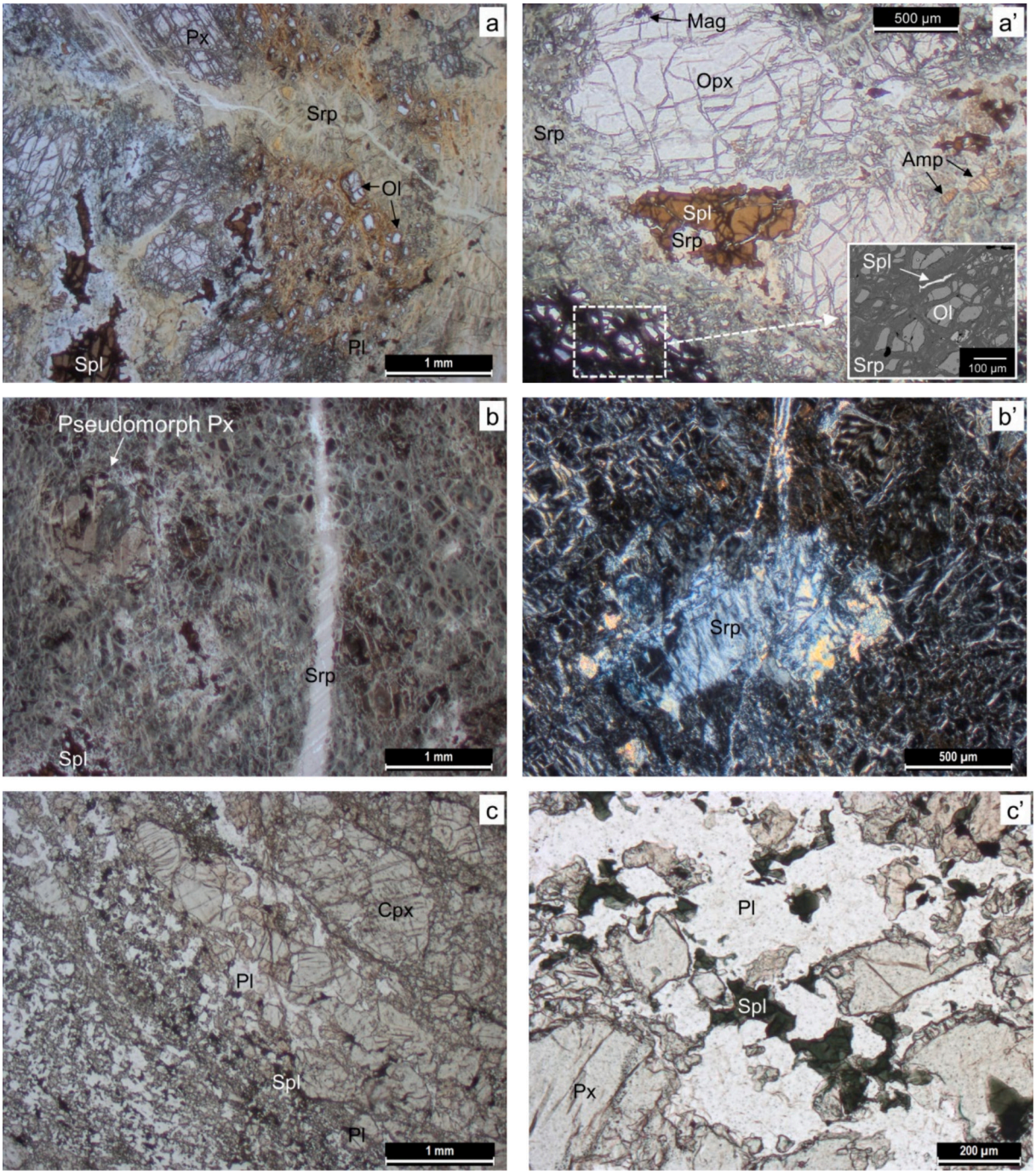


Fig. 2. Thin-section photomicrographs of peridotites (a-a'), serpentinites (b-b'), and pyroxenites (c-c'), all taken under plane-polarized light, except for b', which is shown under cross-polarized light. a) Pyroxene porphyroclasts set in a fine-grained matrix mainly composed of serpentine with a mesh texture and relict olivine cores (sample VAF-6). a') Orthopyroxene and spinel porphyroclasts with brown amphibole in a fine-grained serpentine matrix; the inset shows a backscattered electron image highlighting mesh texture in detail, (sample VAF-4a). b) and b') Pseudomorph of pyroxene immersed in a serpentine matrix cut by serpentine veins, locally forming fibrous patches (sample VAF-7a). c) Pyroxenite exhibiting fine-grained layers intercalated with coarser grains, which are mainly composed of clinopyroxene (sample AM-483). c') Sample AM-403, which illustrates in detail the pyroxenite sample's texture, showing interstitial green Al-spinel and plagioclase surrounded by pyroxene crystals. Amp: Amphibole; Cpx: clinopyroxene; Mag: magnetite; Ol: olivine; Opx: orthopyroxene; Pl: plagioclase; Px: pyroxene; Srp: serpentine; Spl: spinel. (For interpretation of the references to colour in this figure legend, the reader is referred to the web version of this article.)

parameter and the solubility products at different temperatures (logK) were calculated in this study using the *calclogKclays* function in PyGCC, which is an updated and implemented version of the ClayTherm tool (Awolayo and Tutolo, 2022; Blanc et al., 2021). The uncertainty in terms of saturation index evaluated on lizardite is ±0.27. In contrast, for magnetite(am), the standard-state thermodynamic parameters were taken from the Thermoddem database (Blanc et al., 2012), while the log K values were calculated using PyGCC. Finally, hypothetical ideal solid solutions between lizardite-greenalite and lizardite-Mg-cronstedtite were calculated using the dedicated function in GWB. Although greenalite and cronstedtite have not been identified as discrete mineral phases in the serpentinite assemblage (see Section 5.2), representing Fe in lizardite as an ideal solid solution between the magnesian end-member (lizardite) and Fe-rich end-members (greenalite and/or cronstedtite) is a robust and widely adopted modeling strategy, supported by mineralogical and thermodynamic studies (Evans et al., 2009; Tutolo et al., 2019). This approach is commonly used when the relative proportions of ferrous and ferric serpentine components cannot be directly quantified.

4. Results

4.1. Petrography and mineral chemistry

The Mt. Prinzera ophiolitic body is mainly composed of peridotites – with variable degrees of serpentinization – serpentinites, and minor pyroxenites.

Lherzolitic peridotites, the mantle protolith of the serpentinized peridotites, are the most abundant rock type in Mt. Prinzera, which comprises the samples AM-288b, AM-372, AM-394, AM-419, VAF-4a, VAF-4b, VAF-5, and VAF-6. They consist of foliated, porphyroclastic rocks characterized by alternating bands enriched in olivine and pyroxenes interlayered with serpentine-dominated zones. The rocks display a well-developed porphyroclastic texture, with large clinopyroxene and orthopyroxene crystals (up to 9 mm) set in a fine-grained serpentinized matrix exhibiting a mesh texture (Fig. 2a). Olivine is variably preserved or entirely replaced by mesh-texture, hourglass-texture, or fibrous-textured serpentine. Pyroxenes commonly exhibit wavy extinction, and mutual exsolution lamellae; brecciated textures have also been observed. Cr-spinel (up to 3 mm) is widespread and typically exhibits a holly-leaf texture. Fibrous serpentine veins (0.1–1 mm wide) crosscut the porphyroclasts and matrix. Fine-grained, disseminated brown amphibole and Fe-Ni-Cu sulfides (pentlandite-chalcopyrite intergrowths) occur as accessory phases, typically associated with pyroxenes. Serpentine dominates the modal composition (45–65 vol%), followed by clinopyroxene (10–20 vol%), orthopyroxene (8–18 vol%), and olivine (8–18 vol%), while Cr-spinel is present in lower amounts, varying from 1 to 5 vol% of the modal abundances. Variable amounts of very fine-grained magnetite (up to 5 vol%) are associated with serpentine, along the mesh rims or as seams in hourglass and fibrous serpentine; relatively coarse-grained magnetite (up to 0.1–0.2 mm) is locally present in serpentine veins (Fig. 2a').

Foliated serpentinites are widespread in the area and represent advanced alteration products of peridotites. The samples VAF-7a and VAF-8 correspond to this lithotype. They are characterized by a serpentine-rich matrix (+magnetite), comprising 90 vol% – 93 vol% of the rock. Brucite has not been identified either optically or by EMPA analysis. Former porphyroclasts of pyroxene and olivine are entirely replaced by serpentine, generally forming pseudomorphic textures (Fig. 2b). Relict clinopyroxene (diopside) is rare (up to 2 vol%), while interstitial Cr-spinel (2–5 vol%) is partially or totally replaced by opaque minerals (ferritchromite). The serpentine matrix displays both mesh and hourglass texture and is crosscut by serpentine veins (0.2–0.8 mm wide), which locally form serpentine patches (Fig. 2b'). Sample VAF-8 contains patches of reddish alteration phases, which suggest late oxidation processes affecting the magnetite associated with serpentine.

Layers of foliated pyroxenites are widespread at Mt. Prinzera, corresponding to samples AM-332, AM-371, AM-403, and AM-483. These rocks display heterogeneous grain size with millimetric to centimetric banding, defined by alternating fine- and medium-coarse-grained zones (Fig. 2c). Clinopyroxene (diopside) is the dominant phase (40–45 vol%), followed by orthopyroxene (enstatite, 15–27 vol%), and interstitial plagioclase (5–25 vol%), which often show wavy extinction. Olivine ($Fo_{85–86}$, 5–8%) is a minor component and typically occurs as fine-grained crystals associated with plagioclase. Green Al-rich spinel (~5 vol%) commonly forms holly-leaf textures (Fig. 2c') or symplectitic intergrowths with pyroxenes. Serpentinization occurs only locally and may affect both olivine and pyroxenes. Few and narrow serpentine veins (up to 0.5 mm) crosscut the rocks. Accessory phases include brown amphibole and Fe-Cu-Ni sulfides (Montanini et al., 2025). Sample AM-332 exhibits petrographic and modal characteristics typical of pyroxenites, including relatively low olivine content and the presence of plagioclase and Al-spinel. However, it also contains a higher proportion of serpentine and a lower abundance of plagioclase compared to other pyroxenite samples (Supplementary Data, Table A). The relative modal abundances of the main mineral phases are determined by visual estimates and are illustrated in Fig. 3. In peridotites, the proportions of clinopyroxene, olivine, and orthopyroxene display a minor variation, while serpentinites and most pyroxenites are enriched in clinopyroxene (Fig. 3a). Overall, spinel is present in low amounts (Fig. 3b); however, its relative abundance is higher in pyroxenites compared to peridotites. In addition, serpentine is notably more abundant in peridotites than in pyroxenites.

Mineral chemistry clearly distinguishes pyroxenites from peridotites (see Table 1 and Supplementary Data, Table B), with serpentinites exhibiting a close similarity to the latter. Peridotites contain olivine with Fo ~ 89 mol% and Cr-spinel (Cr# = 10–34), whereas pyroxenites are characterized by olivine (Fo ~ 85 mol%) and Al-rich Cr-poor spinel. Clinopyroxenes in all lithotypes correspond to diopside; however, those in peridotites and serpentinites display higher Mg# values (88.5–93.1) and are markedly enriched in Cr_2O_3 (0.5–1.3 wt%) compared to those in pyroxenites. Orthopyroxene (enstatite) and Ti-rich amphibole are present in all lithotypes, displaying only minor chemical variations, with Mg# values being slightly higher in peridotites. The chemical composition of serpentine does not display consistent variation among lithotypes; however, it usually reflects its paragenetic context, whether occurring within veins, in the matrix, along spinel rims, or as a replacement of precursor mineral phases (Fig. 4). Serpentine derived from olivine retains the geochemical signature of its precursor, showing relatively high contents of MgO (> 34 wt%) and NiO (most >0.2 wt%) compared to serpentine formed from pyroxenes. Serpentines derived from orthopyroxene have lower NiO (< 0.1 wt%) and MgO (< 34 wt%) but lower Al_2O_3 (> 1.5 wt%) relative to those replacing clinopyroxene, which typically contain higher NiO (> 0.3 wt%) and MgO (> 33 wt%), and lower Al_2O_3 (mostly <1.5 wt%). Serpentine surrounding spinel is enriched in Al_2O_3 (> 3.9 wt%) and depleted in FeOt (< 5 wt%) and NiO (< 0.07 wt%) relative to other serpentine occurrences. Matrix-hosted serpentine does not exhibit a distinctive chemical signature, whereas vein-hosted serpentine is depleted in Al_2O_3 (< 2.8 wt%) and NiO (< 0.13 wt%).

4.2. Whole-rock chemistry

Whole-rock data reveal distinct compositional trends among the three main lithotypes across multiple variation diagrams. The peridotites exhibit a relatively homogeneous chemical composition, with SiO_2 contents ranging from 45 wt% to 47 wt%, Al_2O_3 from 2.7 wt% to 5 wt%, MgO from 39 wt% to 40 wt%, and CaO from 1.6 wt% to 3.8 wt%. They also display consistently high Mg# (~ 90) and low concentrations (<0.25 wt%) of TiO_2, MnO, Na_2O, K_2O, and P_2O_5 (Figs. 5 a-d, Supplementary Data, Table C). The serpentinites show broadly similar compositions, with lower CaO contents (0.4–0.7 wt%) and slightly higher MgO (41–43 wt%). In the CaO vs MgO diagram (Fig. 5a), peridotites,

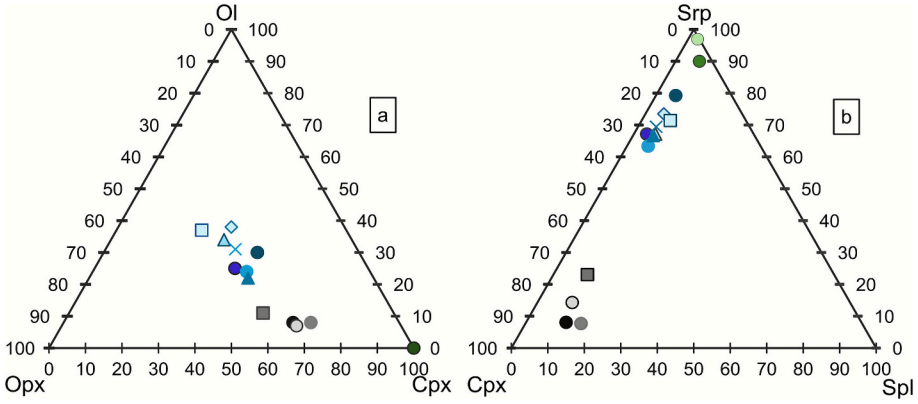


Fig. 3. Ternary diagrams of modal composition of Fe-bearing minerals. a) Ol-Opx-Cpx diagram shows serpentinites and most pyroxenites enriched in Cpx, while peridotites contain a mixture of Cpx, Opx, and Ol. (b) The Ol-Opx-Spl diagram illustrates pyroxenites with higher relative spinel content, compared to peridotites. Note that these modal compositions reflect the current amounts of those minerals and do not represent the original composition of the rocks prior to serpentinization. Blue symbols correspond to peridotites, gray to pyroxenites, and green to serpentinites. Location and sample names are shown in Fig. 1. (For interpretation of the references to colour in this figure legend, the reader is referred to the web version of this article.)

Table 1
Mineral chemistry of peridotites, serpentinites, and pyroxenites, based on EMPA analyses.

	Peridotite	Serpentinite	Pyroxenite
Olivine	Fo = 88.8–90.4 (mol %)	(not measured)	Fo = 85.0–85.4 (mol %)
Clinopyroxene	Diopside (Cr-rich and higher Mg#)	Diopside (Cr-rich and higher Mg#)	Diopside (Cr-poor and lower Mg#)
Spinel	Cr-Spinel	Cr-spinel, ferritchromite	Al-spinel
Orthopyroxene	Enstatite	Enstatite	Enstatite
Amphibole	Ti-rich amphibole	(not measured)	Ti-rich amphibole

pyroxenites, and serpentinites form distinct clusters. In contrast, in the Al_2O_3 vs SiO_2 diagram (Fig. 5b), peridotites are clearly separated from pyroxenites, although they remain geochemically similar to serpentinites. The chemical compositions of the peridotites and serpentinites are aligned to the terrestrial mantle array in the MgO/SiO_2 vs Al_2O_3/SiO_2 diagram (Fig. 5d). Accordingly, the serpentinization did not significantly modify these elemental ratios.

Pyroxenite samples are clearly enriched in Al_2O_3 (~15 wt%), SiO_2 (~ 47 wt%), and CaO (12–14 wt%), while exhibiting significantly lower MgO (12–17 wt%) compared to the peridotites. Notably, sample (AM-332) shows an intermediate composition, with CaO at 7.2 wt%, Al_2O_3 at 8.3 wt%, and MgO at 27.9 wt%, along with relatively high SiO_2 and TiO_2 contents (Fig. 5b and c). Despite its transitional composition, AM-332 retains Mg# comparable to that of peridotites. In the TiO_2 vs Mg# diagram (Fig. 5c), pyroxenites show a broader range in both parameters, with AM-332 standing out for its elevated TiO_2.

4.3. Bulk and mineral-scale iron quantification

Total Fe content ($FeO + Fe_2O_3$) in whole-rock ranges from 7.39 wt% to 9.48 wt% (Fig. 6a). Concentrations of Fe_2O_3 vary between 1.87 wt% and 6.32 wt%, whereas FeO content ranges from 2.85 wt% to 6.48 wt%. Samples AM-371 and VAF-4a contain the highest amounts of divalent Fe (6.48 wt% and 6.42 wt%, respectively), while samples VAF-8 and VAF-4b show the highest level of trivalent Fe (6.32 wt% and 4.80 wt%, respectively).

Both the LOI (Loss of Ignition) values and the serpentine modal amounts, used as a proxy for the degree of serpentinization, vary

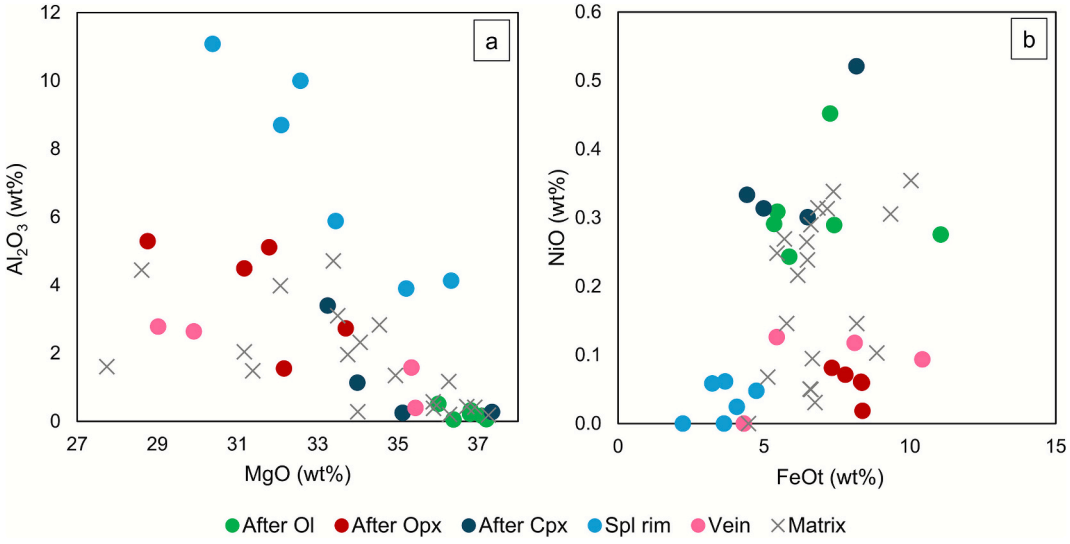


Fig. 4. Variation diagrams of serpentine composition analyzed by EMPA, illustrating the influence of the replaced mineral phase and occurrence in veins. a) Al_2O_3 vs MgO diagram. b) NiO vs FeOt diagram. Total Fe is expressed as FeOt (wt%).

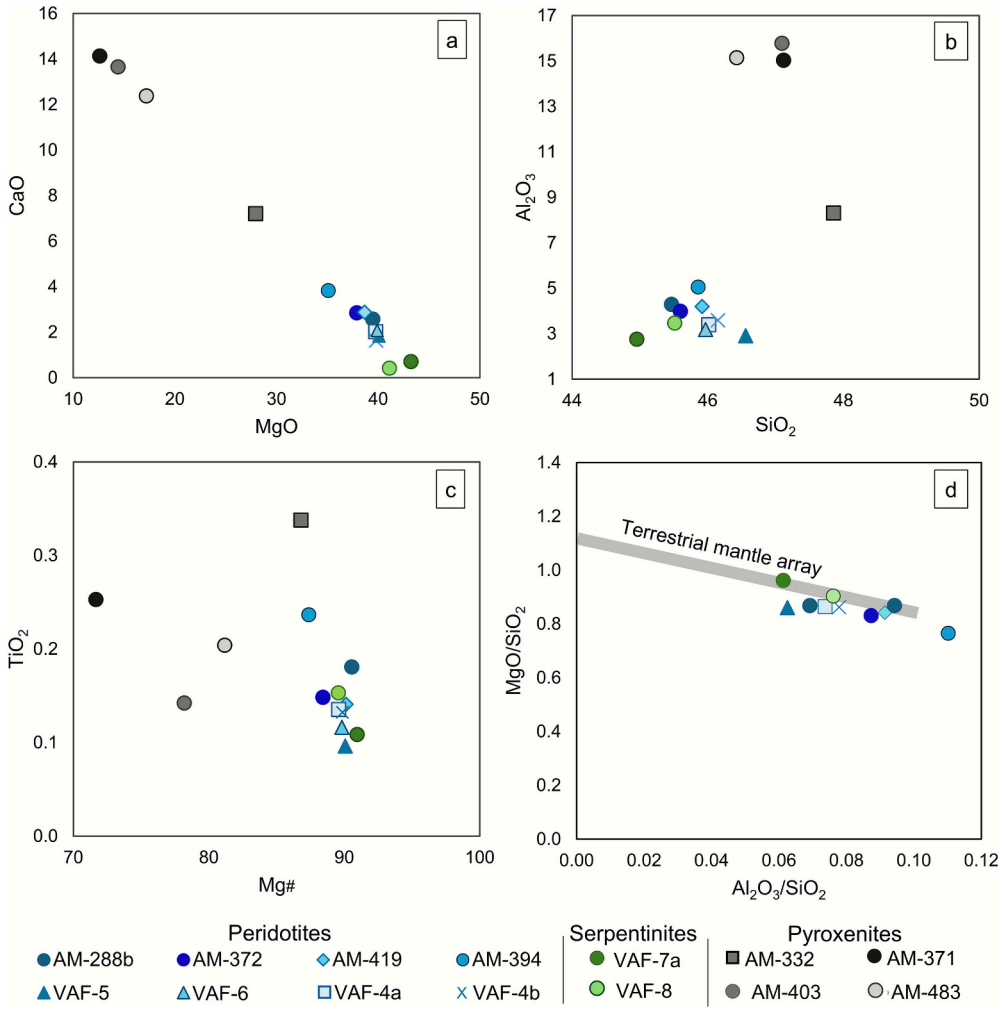


Fig. 5. Variation diagrams for whole-rock compositions of ultramafic rocks from Mt. Prinzera. a) CaO versus MgO (wt%) diagram illustrates chemical variation among three lithotypes. b) Al_2O_3 versus SiO_2 (wt%) diagram clearly differentiates peridotites from pyroxenites, though it does not effectively distinguish serpentinites from peridotites. c) TiO_2 (wt%) versus Mg# diagram shows greater variability on these elements for pyroxenites, while peridotites and serpentinites exhibit similar Mg# and TiO_2 values. d) MgO/SiO_2 (wt%) vs Al_2O_3/SiO_2 (wt%) diagram for the peridotite and serpentinite samples of Mt. Prinzera. The terrestrial mantle array is taken from Jagoutz et al. (1979) and Hart and Zindler (1986).

considerably among lithotypes from Mt. Prinzera. Pyroxenites show a relatively low degree of serpentinization (< 15 vol% of serpentine and < 5.1 wt% of LOI), peridotites show intermediate values (45–65 vol% of serpentine and 7.1–13.1 wt% of LOI), and serpentinites show much higher content (> 90 vol% of serpentine and > 14.2 wt% of LOI). The degree of serpentinization shows an inverse relationship with FeO content across lithotypes (Fig. 6b) and a direct relationship with Fe_2O_3 amounts. Pyroxenites, which are the least altered, tend to exhibit higher FeO and lower Fe_2O_3 contents, while peridotites and serpentinites, which are more altered, display lower concentrations of FeO, comparable to their Fe_2O_3 values (Fig. 6b). However, some deviations from this trend are observed. For instance, sample VAF-4a, a peridotite preserving mantle foliation, despite its ~50 vol% serpentinization, shows relatively high FeO content and very low Fe_2O_3 concentrations. Conversely, sample AM-483, a weakly serpentinized pyroxenite (~ 10 vol%), contains FeO and Fe_2O_3 levels comparable to those of more altered peridotites.

Major element oxide concentrations vary by lithology, as expected. Peridotites and serpentinites are characterized by elevated MgO (35–43 wt%), whereas pyroxenites are enriched in CaO (12–14 wt%), Al_2O_3 (~ 15 wt%), and Na_2O (1.1–1.5 wt%). Among the pyroxenites, samples with high amounts of Fe^{2+} (AM-332 and AM-371) show no significant variation in most major oxide composition compared to those with lower FeO levels. Similarly, the Fe^{2+}-rich peridotite VAF-4a exhibits a chemical profile consistent with other peridotites (Fig. 6c).

4.4. Fe distribution within host phases

Mössbauer spectroscopy was employed mainly to determine the iron valence states within the primary rock-forming minerals. The Fe^{2+}-bearing phases identified include olivine, clinopyroxene, orthopyroxene, amphibole (only in sample AM-394), serpentine, and spinel. Fe^{3+} was detected exclusively in the serpentine structure (Fig. 7; Table 2).

The doublet observed in sample VAF-4a, with an isomer shift (δ) of 0.66 mm/s and no quadrupole split (QS), was interpreted as magnetite $Fe^{2.5+}$ at the octahedral site, resulting from electron hopping between Fe^{2+} and Fe^{3+} (Geymond et al., 2025). Magnetite typically appears as sextets in Mössbauer spectra; however, in cases of tiny crystals or poor crystallinity, these sextets may collapse into doublets (Cao et al., 1997; Goneková et al., 2020).

Mössbauer spectroscopy is sensitive to Fe-bearing minerals with iron contents as low as 1 wt% (Waanders, 2013), which represent a significant fraction of the total iron-bearing phases in a sample. Consequently, plagioclase – although comprising 25 vol% of sample AM-371 – was not detected due to its low or negligible iron content. Magnetite, present as a minor phase, was identified only in sample VAF-4a due to its low

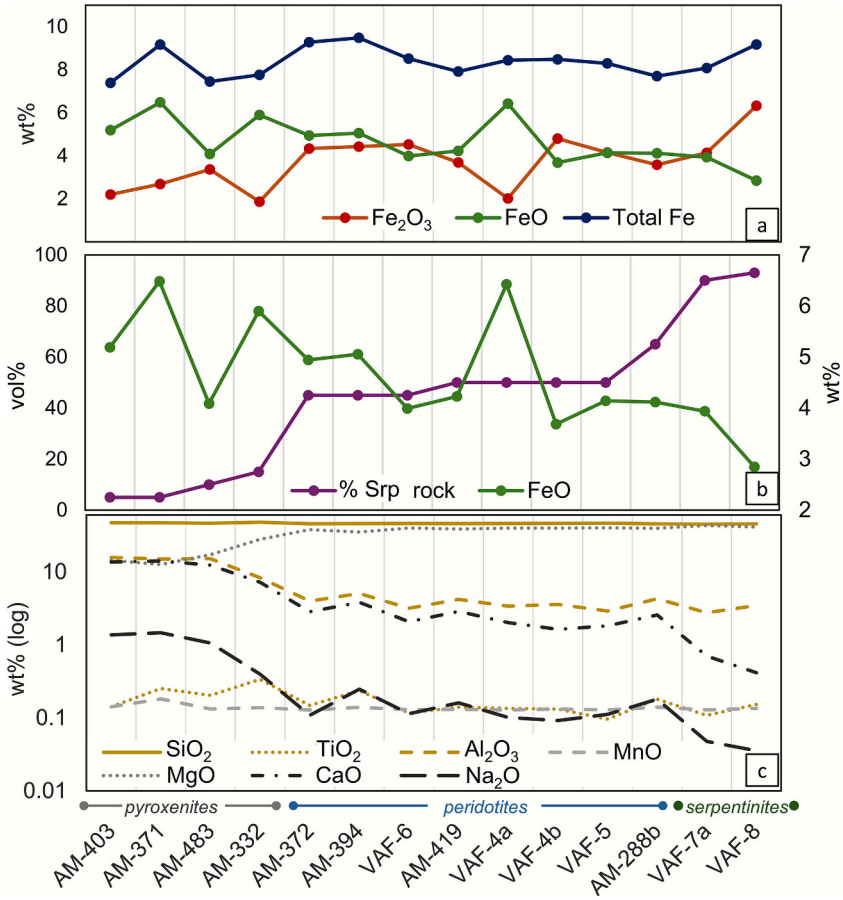


Fig. 6. Multi-panel geochemical diagrams of the pyroxenite, peridotite, and serpentinite samples, ordered along the x-axis. a) Iron specification shown as FeO, and Fe_2O_3, and total Fe, all in wt%. b) Degree of serpentinization (% Srp rock) and FeO content (wt%). c) Log-scale concentrations of major element oxides.

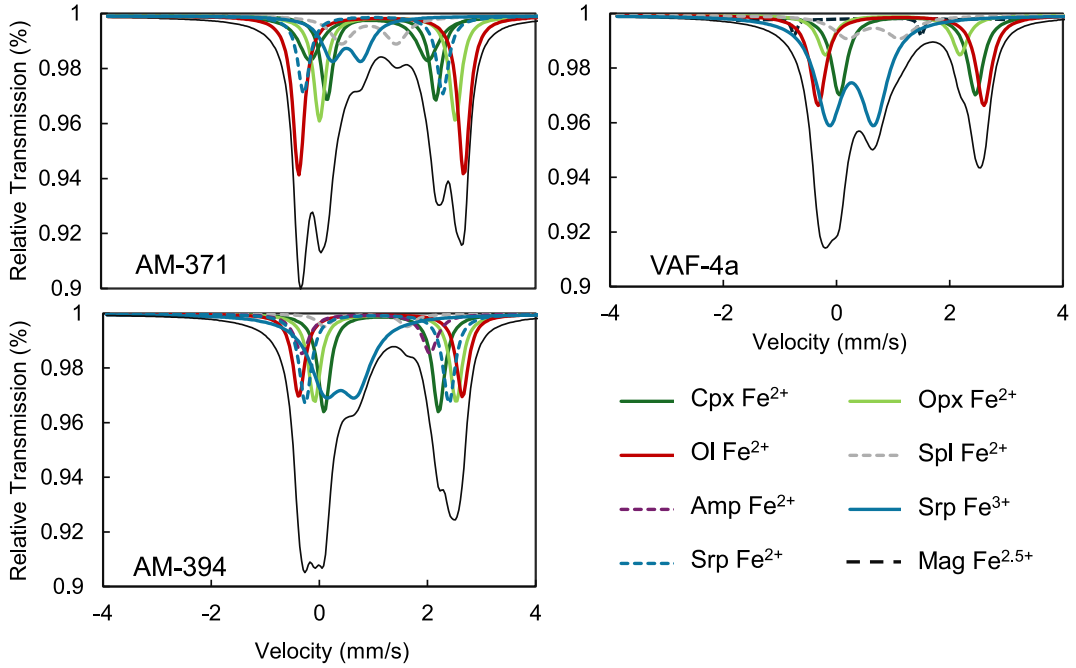


Fig. 7. Mössbauer spectra fittings for samples AM-371, AM-394, and VAF-4a, conducted at low velocity (from −4 to 4 mm/s) and room temperature (295 K) in a zero magnetic field.

abundance in samples AM-371 and AM-394 (up to 1 vol%). Similarly, Mössbauer spectroscopy further supported the absence of brucite, which

Table 2
Hyperfine parameters, including isomer shift (δ) and quadrupole splitting (QS), were used to determine the mineral phase contributions and their corresponding valence states. Reference values are based on Geymond et al. (2025), except for brucite (not present in that study), for which parameters from Binfu and Yilong (1999) were used. Iron coordination within the mineral lattice is indicated as octahedral (M) or tetrahedral (T). Measure uncertainties are ±0.00–0.03 mm/s for the isomer shift (δ), ± 0.001–0.09 mm/s for quadrupole splitting (QS), and ± 0.00–0.008 for relative area (RA). (*) magnetite 2.5^{+} corresponds to electron hopping between Fe^{2+} and Fe^{3+} at the octahedral site. X^2 corresponds to the mean-square displacement of the Mössbauer probe nucleus in the crystal lattice (Rancourt, 1998).

Sample	Contribution	Fe valence	δ (mm/s)	QS (mm/s)	RA (%)	χ2	Mössbauer Bulk $Fe^{2+}/\Sigma Fe$	Titration Bulk Fe2+/ΣFe
AM-371 (pyroxenite)	Olivine M1	2^{+}	1.16	3.04	25	0.27	0.89	0.73
	Clinopyroxene M1	2^{+}	1.16	2.00	13			
	Clinopyroxene M2	2^{+}	0.93	2.17	13			
	Orthopyroxene M1	2^{+}	1.27	2.50	17			
	Serpentine M	3^{+}	0.52	0.54	11			
	Serpentine M	2^{+}	1.01	2.56	12			
	Spinel T	2^{+}	0.93	1.01	8			
AM-394 (peridotite)	Olivine M1	2^{+}	1.13	3.03	14	0.37	0.72	0.56
	Clinopyroxene M2	2^{+}	1.15	2.12	17			
	Orthopyroxene M1	2^{+}	1.22	2.62	15			
	Serpentine M	3^{+}	0.39	0.58	28			
	Serpentine M	2^{+}	1.07	2.66	15			
	Spinel T	2^{+}	0.86	1.53	3			
	Amphibole M3	2^{+}	0.86	2.37	8			
VAF-4a (peridotite)	Olivine M1	2^{+}	1.15	2.93	19	0.38	0.60	0.78
	Clinopyroxene M2	2^{+}	1.00	2.40	10			
	Orthopyroxene M1	2^{+}	1.26	2.42	20			
	Serpentine M	3^{+}	0.26	0.81	40			
	Spinel T	2^{+}	0.65	0.86	10			
	Magnetite	2.5^{+} (*)	0.66	–	1			

was not identified by any other analytical method.

The $Fe^{2+}/\Sigma Fe$ ratio for the bulk-rock was estimated using Mössbauer Spectroscopy, based on the relative area of each mineral and its iron oxidation state. These results were compared to the bulk-rock titration values (Table 2). For sample VAF-4a, the Mössbauer-derived ratio was lower than that obtained by titration, whereas for samples AM-371 and AM-394, it was higher. The deviation between the two methods ranged from ±16% and ± 18%. This variation is expected, as Mössbauer spectroscopy results are influenced by the choice of fitting parameters and programs used to fit the Mössbauer spectra (Dyar et al., 2006). While titration may provide more accurate bulk $Fe^{2+}/\Sigma Fe$ ratios, Mössbauer spectroscopy offers a valuable first-order approach for identifying Fe-bearing phases and their oxidation states.

For samples AM-394 and VAF-4a, the modal compositions obtained from microscopy (Supplementary Data, Table A) are consistent with the estimates based on relative area from Mössbauer spectroscopy (RA; Table 2). In contrast, sample AM-371 shows discrepancies, with Mössbauer results indicating higher olivine and serpentine contents than the petrographic analysis. Notably, plagioclase – representing 25 vol% of the rock – is absent in the Mössbauer spectra, as it is not a Fe-hosting phase, which may partially explain the discrepancy between the two methods.

5. Discussion

During their geological evolution, peridotites and pyroxenites of Mt. Prinzera experienced multiple stages of retrograde hydration under brittle conditions, leading to significant changes to the mineral assemblages (Montanini et al., 2006). Serpentinization is the most widespread and prominent of these events, with textural relationships indicating that it occurred as a polyphase process. Each alteration stage could have the potential to produce H_2 through the alteration of both the primary and secondary mineralogy of peridotites and pyroxenites (Lévy et al., 2022).

5.1. Early serpentinization stages

The mantle body of Mt. Prinzera experienced anhydrous evolution at high temperatures (ca. 1100–700 °C) during its exhumation from the lowermost lithospheric levels (Montanini et al., 2006). This process occurred in response to Mesozoic lithospheric thinning, along a decompression path from ~2.8 GPa to 0.4 GPa (Ferrari et al., 2022). Subsequently, the studied ultramafic rocks, like other mantle bodies from the Northern Apennines ophiolites, were subjected to complex alteration processes, including multiple stages of serpentinization, carbonation, and metasomatism during their final uplift to the seafloor (see also Schwarzenbach et al., 2021). Among these, serpentinization plays a key role in modifying mineralogy and redox state, potentially generating H_2. Therefore, understanding these fluid-rock interactions is essential for evaluating their potential for H_2 production.

The oldest serpentinization events, attributed to extensive fluid circulation during Jurassic rifting and continental breakup (Montanini et al., 2006), were responsible for diffuse veining and alteration of primary rock-forming minerals (Fig. 8). Olivine was the most intensively altered mineral. Fresh olivine grains are rare, with most occurrences consisting of partially preserved crystals or relic cores embedded within a mesh serpentine matrix. As the degree of serpentinization increases from ~45 vol% to ~65 vol%, there is a marked decrease in the abundance of olivine porphyroclasts and relict cores, reflecting progressive mineral replacement. In serpentinites showing over 90 vol% of serpentinization degree, olivine relics are no longer observed, indicating a total transformation of the primary mineral assemblage.

Fresh orthopyroxene occurs in pyroxenites and peridotites. In peridotites, however, it is often partially altered along grain boundaries or completely replaced by bastite. In the current modal composition, orthopyroxene is generally less abundant than clinopyroxene and exhibits a more advanced stage of alteration. Similar to olivine, orthopyroxene is completely replaced by serpentine in serpentinites, occasionally preserving a pseudomorphic textures.

Clinopyroxene is relatively resistant to alteration and is currently the most abundant primary phase in pyroxenites and peridotites. In serpentinites, a few relict porphyroclasts of clinopyroxene are still

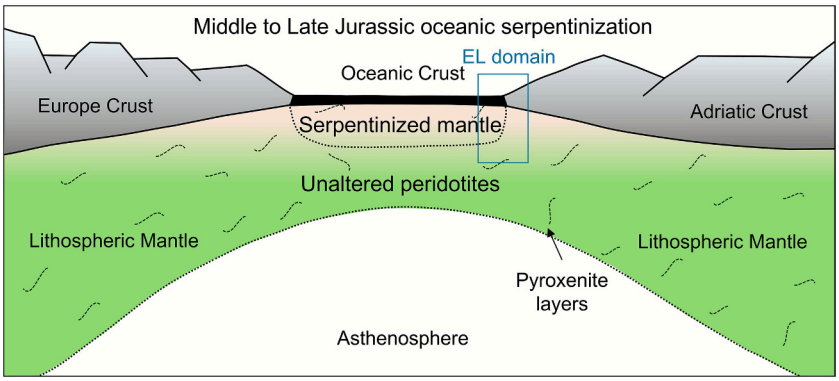


Fig. 8. Schematic profile (not to scale) illustrating mantle serpentinization in the Ligure-Piemontese basin during the Middle-Late Jurassic. Modified from Montanini et al. (2006) and Piccardo et al. (2009). EL corresponds to External Ligurian.

preserved, which highlights their relative stability during serpentinization.

Among the primary rock-forming minerals, spinel is the most resistant to alteration, and it can be preserved as porphyroclasts also in serpentinites. The alteration is generally limited to the grain margins.

Reactions involving the serpentinization of olivine and pyroxene, as outlined in Eqs. 1 and 2 (Section 1), together with the observed mineral assemblages and their iron speciation, described in Section 4.4, provide critical insights into iron partitioning during serpentinization. The oxidation process involves Fe^{2+} originally hosted in olivine and pyroxene structures, which is oxidized to Fe^{3+} within serpentine minerals, likely generating H_2. The absence of brucite which could imply Fe^{2+} sequestration in this phase, potentially enhanced iron oxidation, and promoted H_2 production.

The presence of spinel may have further enhanced H_2 production, potentially acting as a catalyst through the release of aluminum during serpentinization (Huang et al., 2015). Mayhew et al. (2013) argued that electron transfer between water and Fe^{2+} adsorbed on spinel surface during alteration of Fe^{2+}-bearing silicates (olivine, pyroxene) can also favor H_2 generation. Moreover, experimental studies have reported that spinel dissolution can accelerate olivine serpentinization by at least a factor of two (Wang et al., 2020; Portella et al., 2024).

The temperature of this serpentinization stage can be estimated based on thermodynamic models. Considering the average protolith composition of Mt. Prinzera peridotite (olivine: 60 vol%, orthopyroxene: 20–30 vol%, clinopyroxene: 10–20 vol%) and the observed secondary assemblage – predominantly serpentine, with minor magnetite, and less altered clinopyroxene – serpentinization likely occurred between 220 °C and 300 °C (Klein et al., 2013). The absence of brucite and the high degree of olivine consumption support this interpretation. Furthermore, the faster alteration rate of olivine compared to orthopyroxene suggests a temperature below 250–300 °C, as pyroxenes are more reactive only at higher temperatures above this threshold (Bach et al., 2004; Ellison et al., 2021, and references therein). These observations suggest that, under low-temperature conditions, serpentinization is primarily driven by olivine rather than pyroxene.

A later alteration stage formed comminuted serpentine (+ carbonates) within the cataclasite matrix at low temperatures (< 50 °C), possibly related to seawater-driven alteration (Montanini et al., 2006). This episode was significantly less extensive, and the associated mineralogical changes are challenging to characterize, rendering the assessment of H_2 generation potential uncertain.

5.2. *Ongoing serpentinization and modern H_2 generation*

The alteration of primary mineral assemblage during the first-stage serpentinization reduced the abundance of Fe^{2+}-bearing minerals in the system, likely decreasing the H_2 generation potential of the present rocks compared to their protoliths. However, the presence of olivine and pyroxene relics suggests that these rocks may still retain the capacity for H_2 production.

Olivine serpentinization can occur at temperatures below 250 °C (Bach et al., 2004), with experimental studies demonstrating that the reaction is possible even at very low temperatures (< 70 °C; Neubeck et al., 2011; Mayhew et al., 2013).

In addition, extensively serpentinized rocks can sustain H_2 generation through alteration of secondary minerals, such as Fe^{2+}-bearing serpentine and brucite (Ellison et al., 2021), and Fe^{2+}-hosting magnetite (Geymond et al., 2023). Mössbauer spectroscopy of the pyroxenite and peridotite samples AM-371 and AM-394 reveals that, during its formation, serpentine incorporated both Fe^{2+} and Fe^{3+}, indicating a potential for continued H_2 generation as Fe^{2+} is further oxidized.

A fresh hyperalkaline spring (TDS = 112 mg/kg; pH = 11.2; Boschetti et al., 2013) discharging at the base of Mt. Prinzera, oversaturated with respect to lizardite, and containing dissolved H_2 (up to 0.79 μM; Freitas et al., 2025) may suggest a possible relationship between hydrogen production and an active subsurface serpentinization process. Compared to the hyperalkaline waters from the Ligurian ophiolites, which appear to be more evolved in terms of water–rock interaction progress (Boschetti and Toscani, 2008), this Mt. Prinzera water represents the compositional transition of the interacting fluid, evolving from an initial, slightly basic Mg–HCO_3-type composition (pH 7.6–8.7; positive redox potentials, Eh) to a hyperalkaline Na–OH-type composition characterized by a low redox value (Eh = −282 mV). During that compositional shift, Mg and dissolved silica are sequestered by neoformed, amorphous serpentine minerals, as supported by reaction-path modeling calculations and saturation indices (Boschetti and Toscani, 2008; Segadelli et al., 2017).

Speciation of the hyperalkaline spring average composition at Mt. Prinzera (Supplementary Data Table D, ion charge balance 2.3%) indicates oversaturation with respect to lizardite solid solutions containing Mg-cronstedtite and greenalite, with lizardite activity close to 0.9 in both cases (Supplementary Material 2, Document B). Activity diagrams substantially support this observation (Fig. 9). Notably, the calculated equilibrium redox potentials for the carbon and hydrogen Nernst redox couples at the physicochemical conditions of the spring are quite similar, i.e., Eh[C(-IV)/C(+IV)] = −0.517 V and Eh[H(0)/H(+I)] = −0.547 V. Very consistent values were obtained using both the GWB and PHREEQCi codes, despite the use of different thermodynamic datasets (llnl.dat for PHREEQCi, version 3.8.7; Parkhurst and Appelo, 2013). The overall redox state of the system, ranging between the values of Eh = −0.53 (likely representative of deeper conditions) and Eh = −0.28 (at the time of sampling), is consistent with equilibrium among lizardite solid solutions containing both Fe^{2+} and Fe^{3+} (Fig. 9b), which also aligns with the model for hydrogen production during serpentinization proposed by Tutolo et al. (2020). Two possible reactions that may

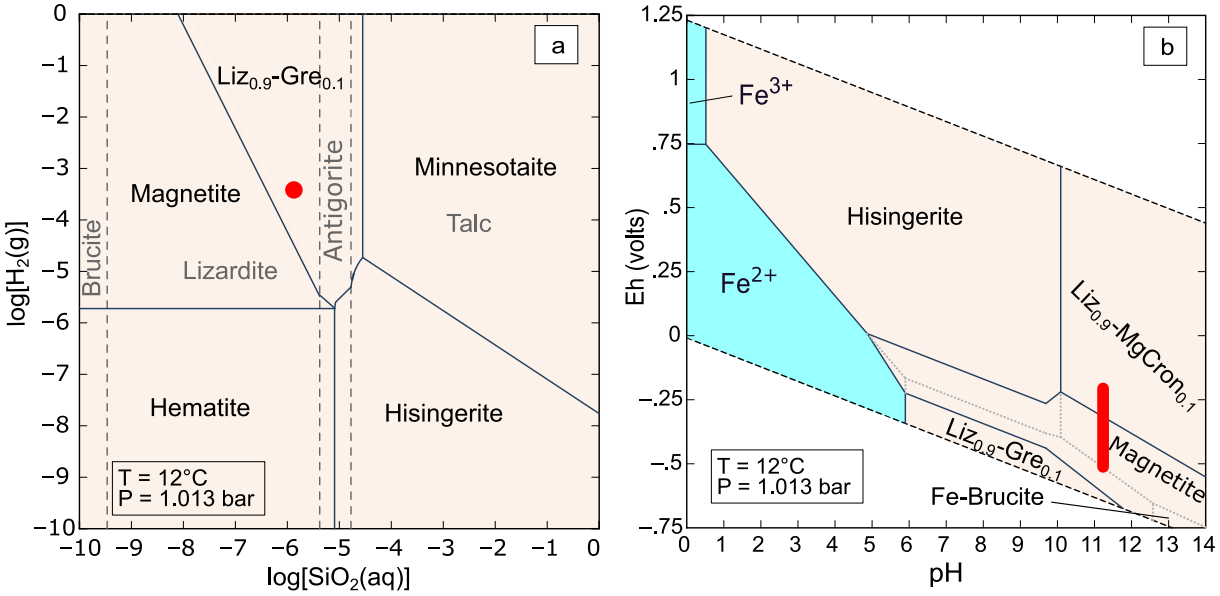


Fig. 9. a) Stability fields of the Fe-Mg-Si-O-H system as a function of H_2(g) fugacity and SiO_2(aq) activity. The vertical dashed lines represent the boundaries between the pure Mg-bearing phases (gray labels). b) Eh-pH diagram of the Fe-Mg-Si-O-H system. The dotted lines indicate phase boundaries calculated excluding magnetite, allowing the appearance of Fe-brucite. In b), hematite was excluded to emphasize the stability fields of the spread of magnetite and serpentine solid-solutions (Liz-Crons is covered by hematite in a). In both diagrams, the red circle (a) and the red vertical bar (b) represent the conditions of the hyperalkaline spring at Mt. Prinzera. Specifically, the top and bottom values of the bar in b) correspond to the measured (−0.28 V) and calculated (−0.53 V) Eh values, respectively, the latter representing the average value obtained from the carbon and hydrogen redox couples (see text for details; Supplementary Material 2, Document B). (For interpretation of the references to colour in this figure legend, the reader is referred to the web version of this article.)

account for active H_2 generation are shown below:

$$\underset{Fe^{2+}\text{-serpentine}}{Mg_{2.7}\,Fe_{0.3}{}^{2+}\,Si_2O_5(OH)_4} + 2.4Fe^{2+} + 4.45\,H_2O = 4.8H^+ + 1.35\underset{Mg-cronstedtite}{Mg_2\,Fe_2{}^{3+}\,SiO_5(OH)_4} + 0.65SiO_2(aq) + 1.35H_2(g) \quad (3)$$

$$\underset{Fe^{2+}\text{-serpentine}}{Mg_{2.7}\,Fe_{0.3}{}^{2+}\,Si_2O_5(OH)_4} + 0.8\underset{magnetite(am)}{Fe_2{}^{3+}Fe^{2+}O_4} + 1.25\,H_2O = 1.35\underset{Mg-cronstedtite}{Mg_2\,Fe_2{}^{3+}\,SiO_5(OH)_4} + 0.65SiO_2(aq) + 0.55H_2(g) \quad (4)$$

In both reactions, the solid solution lizardite(0.9)-greenalite(0.1) is called Fe^{2+}-serpentine according to Tutolo et al. (2020), and treated here as pure, singular solid species. In Eq. (4), an amorphous magnetite buffers the dissolved Fe^{2+}, which instead is represented as a free ion in Eq. (3). Using activity values for aqueous species, water, hydrogen fugacity, Fe^{2+}-serpentine and Mg-cronstedtite in solid solutions with lizardite ($a \approx 0.1$), as derived from speciation modeling and saturation indices of the average hyperalkaline water composition, the calculated thermodynamic equilibrium temperatures (i.e., when the activity product equals the solubility product) are 17 °C for Eq. (3) and 22 °C for Eq. (4) (Supplementary Material 3, Document C). It should also be noted that if an orthopyroxene ($En_{0.9}$) is substituted for Fe^{2+}-serpentine, both reactions (3) and (4) shift toward the right-hand side, favoring product formation. This observation confirms, as previously demonstrated by reaction-path modeling, that the low evolutionary degree of the Mt. Prinzera hyperalkaline water does not allow equilibrium with orthopyroxene to be attained, unlike the more evolved Ligurian ophiolitic waters (Boschetti and Toscani, 2008). The estimated temperature range is consistent with that reported by Bruni et al. (2002) for the hyperalkaline springs of the Ligurian ophiolites (12–25 °C). However, further data is required better to constrain the temperature conditions of this modern process, for example using clumped-isotope on molecular hydrogen (e.g., Mangenot et al., 2023).

Based on the estimated temperature range (17–22 °C), the measured spring temperature at the surface (11.9 °C), and the estimated regional geothermal gradient of 21.2 °C/km (Acosta et al., 2024), active serpentinization at Mt. Prinzera is inferred to occur at depths of 240–480 m (Fig. 10). Similar to the alkaline springs in Liguria, the local climatic conditions have no significant influence on the spring sampling temperatures (Chavagnac et al., 2013; Cipolli et al., 2004). Considering that the maximum estimated thickness of the Mt. Prinzera ultramafic body is

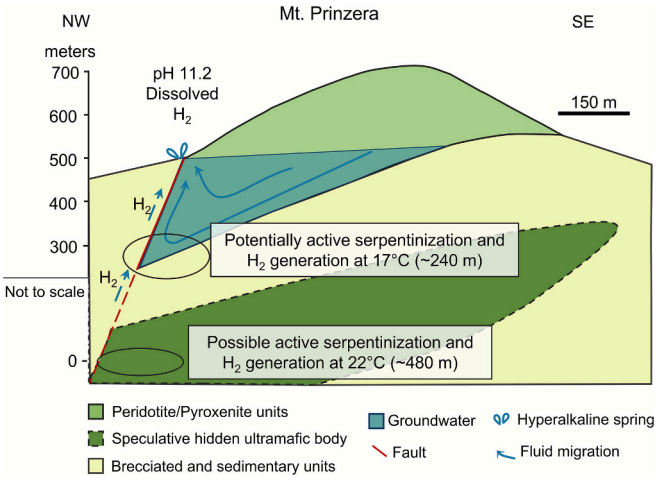


Fig. 10. Ongoing serpentinization at Mt. Prinzera is illustrated by two scenarios: minimum (17 °C) and maximum (22 °C) temperatures derived from thermodynamic calculations. Considering the maximum thickness of 250 m, proposed for the massif (Segadelli et al., 2017), the minimum temperature could be reached within the Mt. Prinzera body. In contrast, the maximum temperature would require an additional source of serpentinization, speculated to be a hidden ultramafic body genetically correlated to those of Mt. Prinzera. The geometry and dimensions of the hidden mantle body remain speculative. Mt. Prinzera geometry and water circulation after Segadelli et al. (2017). Dashed lines correspond to uncertain limits. The vertical scale corresponds to meters above sea level (m.a.s.l.).

about 250 m (Segadelli et al., 2017), active serpentinization at its base could account for the dissolved H_2 measured at the surface. At greater depths, it can be hypothesized that H_2 is generated by the ongoing serpentinization of hidden ultramafic bodies, starting from the base of the body at ~250 m down to a depth of 480 m. The presence of multiple mantle bodies exposed in the region (e.g., Rocca Galgana, Mt. Zirone, Rio Strega), which display similar mineralogical, textural, and genetic features correlate with those of Mt. Prinzera (Lasagna et al., 2005), supports the presence of hidden mantle bodies. The occurrence of Ligurian units, which host the ophiolitic bodies, beneath the Tuscan units in the Pontremoli exploration well (35 km SSW of Mt. Prinzera), at depths greater than 1 km (Artoni et al., 1992), further supports this interpretation. Furthermore, the ultramafic body may be thicker than previously estimated, as already discussed in Freitas et al. (2025), extending to depths of ~480 m. This would allow the highest serpentinization temperatures to likely occur within its interior.

Fluids generated at different depths could migrate along faults to the surface. Field observations and previous studies have identified a set of faults crossing Mt. Prinzera, including one near the hyperalkaline spring (Fig. 10; Segadelli et al., 2017).

Additionally, regarding the mineral assemblage predicted to be associated with the current serpentinization process, i.e., lizardite, magnetite, greenalite, and cronstedtite, the petrographic studies identified serpentine-like minerals and magnetite. The serpentine-like phases correspond mainly to lizardite (see also Montanini et al., 2006). Minerals with chemical compositions compatible with greenalite and cronstedtite were not identified; however, if present, they are likely to represent only a minor proportion of the rock volume, which makes their recognition challenging even using advanced analytical techniques (e.g., see Rivard et al., 2013). The ongoing serpentinization may affect peridotites and serpentinites more significantly than pyroxenites, as indicated by the limited presence of serpentine-like minerals and the absence or scarcity of magnetite in these latter rocks.

A current serpentinization related hypothesis for the presence of H_2 in the sodium-sulfate hyperalkaline spring (Prin2) is reinforced by the absence of detectable H_2 in most of other Mg bicarbonate waters at Mt. Prinzera. However, Freitas et al. (2025) also reported the presence of dissolved H_2 in one of the Mg bicarbonate springs, located on the western side of Mt. Prinzera (Fig. 1). This observation could suggest an alternative hypothesis involving the presence of trapped H_2 accumulations originating from earlier serpentinization stages. Such a serpentinization process is likely to have occurred from the Paleocene onward, when the Apenninic stacking and formation of reservoirs and traps had started, rather than during the more prominent Jurassic serpentinization event that affected these rocks.

5.3. *Additional constraints from isotopic composition: Kinetic vs. equilibrium effects*

The isotopic signature of dissolved methane in the hyperalkaline spring at Mt. Prinzera was $\delta^{13}C(CH_4) = -56.6 \pm 1.6‰$ (Freitas et al., 2025) and $\delta^{2}H(CH_4) = -200‰$ (Boschetti et al., 2013), deviating from abiogenic/abiotic values typically associated with Fischer–-Tropsch–type processes in aquifers hosted by serpentinized ultramafic rocks. Indeed, these isotopic values of methane fall between the thermogenic and microbial fields (Milkov and Etiope, 2018; Ni et al., 2025). However, the hydrogen isotopic compositions of methane and water at Mt. Prinzera hyperalkaline spring, i.e., $\delta^{2}H(H_2O) = -64.5 \pm 0.6‰$ (Segadelli et al., 2017; Segadelli, 2014), are consistent with hydrogenotrophic methanogenesis (Fig. 11a; van Dam et al., 2025; Vinson et al., 2017). Since this process is bacterially mediated, isotopic equilibrium fractionation factors cannot be used to estimate the temperature of the water at depth.

Additionally, estimating the isotopic composition of CO_2 from DIC (Dissolved Inorganic Carbon) in high pH waters may be affected by the kinetic effects associated with hydroxylation reactions (Clark et al., 1992; Christensen et al., 2021). For the hyperalkaline water at Mt. Prinzera, considering $\delta^{13}C(DIC) = -19.3 \pm 0.1‰$ (Barozzi, 2019), if a purely kinetic isotopic depletion due to hydroxylation of −17.1‰ is assumed (Christensen et al., 2021), the estimated $\delta^{13}C(CO_2)g$ value is −2.2‰. In contrast, using the Netpath code (Barbieri et al., 2020; Parkhurst and Charlton, 2008; Plummer et al., 1994), which considers equilibrium fractionation among C(+IV) species as well as the physicochemical properties of the water, a value of $\delta^{13}C(CO_2)g = +7.051‰$ is obtained. Thus, an average value that accounts for both effects is $\delta^{13}C(CO_2)g = +2.43‰$.

The resulting $\Delta^{13}C(CH_4–CO_2)$, calculated as the difference between $\delta^{13}C(CH_4) = -56.6 \pm 1.6‰$ and $\delta^{13}C(CO_2) = +2.43‰$, is approximately $-59 \pm 2‰$. Using the empirical relationship between temperature and bacterial isotope fractionation factors associated with hydrogenotrophic methanogenesis, as constrained by marine sediments data and laboratory experiments (Balabane et al., 1987), this would correspond to a

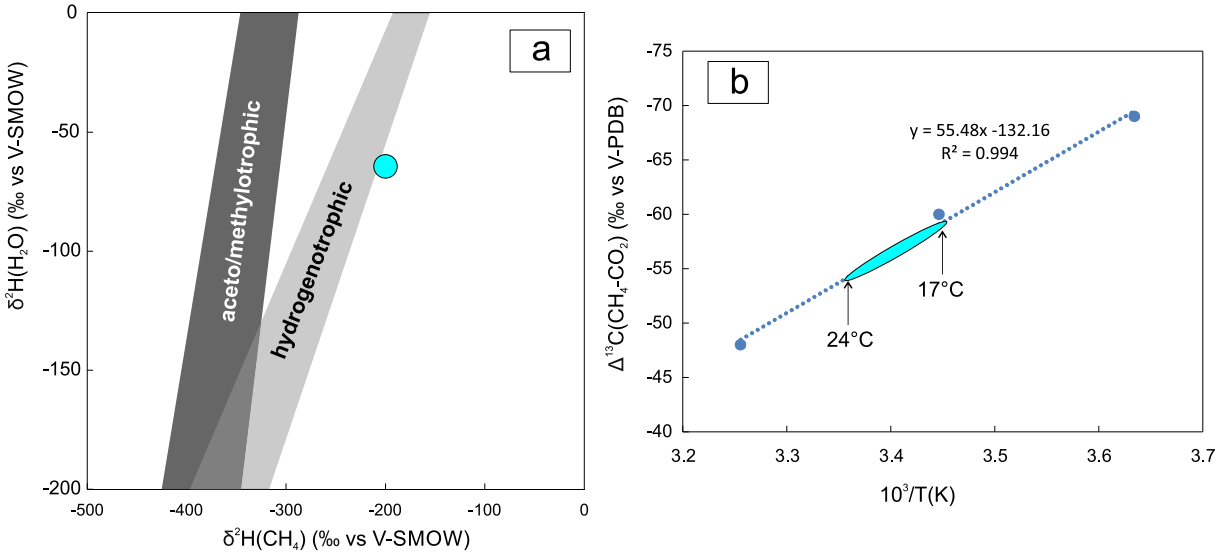


Fig. 11. Diagrams illustrating the isotopic composition of the hyperalkaline spring at Mt. Prinzera (light blue circle/ellipse). a) $\delta^{2}H(H_2O)$ vs. $\delta^{13}C(CH_4)$ diagram, with hydrogenotrophic and aceto/ methylotrophic fields (van Dam et al., 2025; Vinson et al., 2017). b) CH_4-CO_2 fractionation factor vs. temperature (Kelvin) (Balabane et al., 1987). (For interpretation of the references to colour in this figure legend, the reader is referred to the web version of this article.)

temperature of 17 ± 2 °C (Fig. 11b). If only the kinetic effect associated with hydroxylation of dissolved C(+IV) species is considered, we obtain $\Delta^{13}C(CH_4–CO_2) = -54 \pm 2‰$, yielding a slightly higher temperature estimate of approximately 24 ± 3 °C (Fig. 11b). These temperature estimates are undeniably subject to uncertainty, as they depend on assumptions regarding the dominant fractionation mechanisms and the applicability of empirically derived relationships to the studied system. Nevertheless, the convergence between the temperature range inferred from isotopic fractionation and that predicted by thermodynamic modeling suggests that both approaches reflect a comparable low-temperature geochemical regime at depth, despite being based on fundamentally different methodologies.

Although CO_2–CH_4 isotopic fractionation does not provide a direct constrain on the temperature of H_2 generation, it can be used as an indirect proxy under the assumption that H_2 production and hydrogenotrophic methanogenesis are coeval and occur within the same physicochemical environment. Therefore, at Mt. Prinzera, reducing conditions and fluid oversaturation with respect to Fe-bearing lizardite and magnetite suggest active water–rock reactions that generate H_2, which create favorable conditions for hydrogenotrophic methanogenesis.

5.4. H_2 generation potential of peridotites and pyroxenites

At Mt. Prinzera, both peridotites and pyroxenites may have contributed to H_2 generation through serpentinization at different stages. Olivine and pyroxene represent the primary minerals undergoing oxidation to generate H_2. However, pressure-temperature conditions during alteration appear to have been more favorable for the serpentinization of peridotites, likely due to their high olivine content. In contrast, pyroxenites, dominated by clinopyroxene and orthopyroxene, exhibit lower degrees of serpentinization (5–15 vol%), likely reflecting their low olivine abundance and suggesting a more limited contribution to H_2 generation.

The relationship between serpentinization degree – also reflected by Loss on Ignition (LOI) – and the iron redox state show a positive correlation between Fe^{3+} content and serpentinization extent, as expected

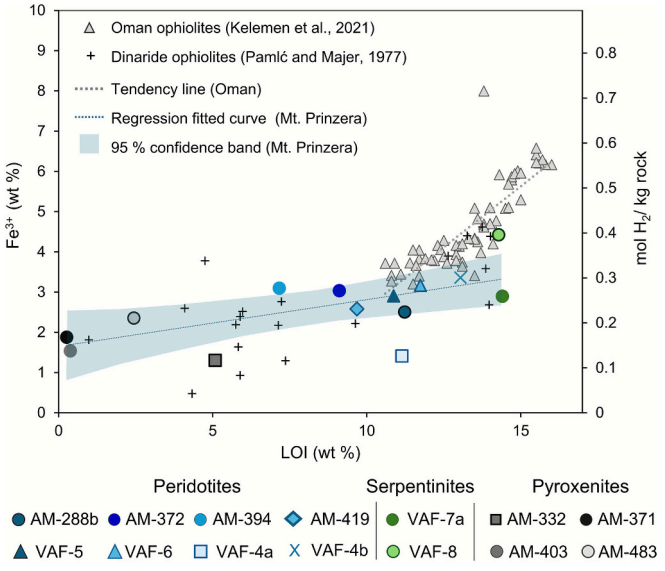


Fig. 12. Oxidized iron (Fe^{3+}, primary axis on the left) and past production of H_2 to date (secondary axis, on the right) versus Loss on Ignition (LOI) from whole-rock analyses of ultramafic rocks from Mt. Prinzera, Samail Ophiolites (Oman; Kelemen et al., 2021), and Dinarides (Bosnia and Herzegovina; Pamlć and Majer, 1977). LOI reflects the weight percentage of H_2O and other volatiles and is used as a proxy for the extent of serpentinization, according to Mayhew and Ellison (2020) and Tutolo and Tosca (2023).

(Fig. 12). The high Fe^{2+} and low Fe^{3+} concentration observed in pyroxenites reflects their limited serpentinization, consistent with the fact that primary minerals such as olivine and pyroxenes contain significantly more FeO than secondary serpentine-group minerals (Klein et al., 2009).

A Deming regression (Boschetti et al., 2019) was performed on the data shown in Fig. 12 to check its consistency, yielding a statistically significant result ($p = 0.0014$). Most samples fall within or near the 95% confidence band. Sample VAF-4a exhibited anomalous values, with the largest residuals, and was considered a potential outlier. This may be due to its markedly lower Fe^{3+}content compared to other peridotite samples with similar modal composition and degrees of serpentinization. The low Fe^{3+} content of sample VAF-4a contrasts not only with its relatively high serpentinization degree, but also with the absence of detected Fe^{2+}-hosting serpentine in the Mössbauer analysis. However, this sample preserves a distinctive texture, retaining its mantle foliation. Sample VAF-4a also contains relatively higher concentrations of magnetite – detected by Mössbauer analysis – occurring not only disseminated within the matrix, as observed in other peridotites, but also as well-formed crystals in veins. This magnetite may have incorporated a greater proportion of Fe^{2+} into its structure, reducing its potential for H_2 generation during the serpentinization.

The Fe^{3+} content of each sample can be used to estimate the amount of H_2 produced per kilogram of rock, based on the reaction: $2\ FeO + H_2O \rightarrow H_2 + Fe_2O_3$, assuming that all Fe^{3+} originates from the oxidation of Fe^{2+} during serpentinization. Whole-rock analyses indicate that the H_2 production potential is generally higher in Oman compared to Mt. Prinzera and Dinaride (Fig. 12). Remarkably, four Dinaride samples follow the upper trend defined by the Oman dataset. At Mt. Prinzera, a single sample (VAF-8) displays a slightly higher inferred H_2 yield, aligning with the Oman trend. However, the elevated Fe^{3+} content of VAF-8 may result from its highly oxidized state, specifically observed in this sample, rather than indicating greater potential for H_2 production.

The potential volume of H_2 generated at Mt. Prinzera over time was estimated by integrating the modal composition of the three main lithotypes with experimentally derived H_2 generation rates, estimated from Fig. 12. The exposed areas approximately cover 0.9 km^2, and assuming an average thickness of 250 m (Segadelli et al., 2017), the total rock volume is estimated to be 225 million m^3. This volume is partially serpentinized, with average fresh rock of 90 vol%, 50 vol%, and 10 vol% for pyroxenites, peridotites, and serpentinites, respectively. Based on field observations, these lithotypes account for approximately 10 vol%, 55 vol%, and 35 vol%, respectively. This yields a total serpentinized volume of approximately 60 vol%, equivalents to 135 million m^3. Assuming an average H_2 generation rate of 0.23 mol H_2 per kilogram of rock (Fig. 12), the total mass of H_2 that could have been produced in this rock volume is estimated at 186,000 t. However, it is noteworthy that the majority of the estimated produced amounts likely derives from the extensive Jurassic serpentinization, whereas only a negligible portion could correspond to ongoing serpentinization.

6. Conclusions

Serpentinization of ultramafic rocks is recognized as one of the main processes responsible for generating natural H_2. The partially serpentinized peridotites and pyroxenites of the External Ligurian units in the Northern Apennines provide a favorable setting for investigating serpentinization processes. Mt. Prinzera is particularly important, as it hosts a hyperalkaline spring containing dissolved H_2, which provides evidence of ongoing reactions and a valuable framework for studying natural H_2 generation. The mineralogical, textural, geochemical, and redox-state characterization of mantle rocks from Mt. Prinzera provides insights into fluid-rock interactions that may have promoted serpentinization and H_2 generation.

Multiple serpentinization phases have been recognized at Mt. Prinzera. The most extensive and pervasive stage is associated with Jurassic

mantle exhumation. This event primarily affected peridotites and, to a lesser extent, pyroxenites, and is recorded by the replacement of primary minerals, such as olivine, clinopyroxene, orthopyroxene, and spinel, with alteration minerals, mainly serpentine, along with minor magnetite, chlorite, and chromite. These reactions likely contributed to H_2 generation, as observed today at mid-ocean ridges. Olivine serpentinization was the most extensive, followed by orthopyroxene, whereas clinopyroxene is the most resistant among the three main primary silicate phases. Spinel, occurring in amounts up to 5 vol%, may have played a catalytic role in serpentinization reactions and H_2 production. The dominance of serpentine as the main secondary phase, the more extensive olivine serpentinization relative to pyroxenes, together with the presence of magnetite (up to 5 vol%) and the lack of brucite, suggest that the Jurassic serpentinization events likely occurred at temperatures ranging from 220 to 300 °C.

Currently, the redox conditions and the oversaturation with respect to (Fe)-bearing lizardite and magnetite in the most evolved hyperalkaline fluid suggest ongoing fluid–rock interactions associated with H_2 generation at Mt. Prinzera. Interestingly, for the hyperalkaline spring at Mt. Prinzera, temperatures inferred from thermodynamic modeling of Fe(II) oxidation and water reduction fall within the range indicated by CO_2–CH_4 isotopic fractionation related to a bacterial methanogenic environments (17–24 °C). Although these estimates are derived from fundamentally different approaches, their convergence suggests that both reflect a comparable low-temperature geochemical regime at depth. At these temperatures, microbial activity probably contributes to maintaining low hydrogen concentrations by continuously consuming H_2. However, as the occurrence of H_2 is not limited to the hyperalkaline spring, fossil H_2 accumulations originating from earlier serpentinization stages may also be considered.

Based on the total volume of serpentinized rocks and the H_2 generation rate inferred from bulk-rock redox data, the total mass of H_2 associated with past and ongoing serpentinization at Mt. Prinzera is estimated to be on the order of 186,000 t. Approximately 40 vol% of the rock volume remain unaltered by serpentinization; however, the current H_2 generation rate per kilogram of rock cannot be reliably quantified, as it is overprinted by the contribution of past serpentinization events. Considering the low and localized concentrations of dissolved H_2 measured in spring waters and the low temperature estimates, the active serpentinization process is likely far less efficient at producing H_2 than the large-scale Jurassic serpentinization events.

CRediT authorship contribution statement

Vivian Azor de Freitas: Writing – review & editing, Writing – original draft, Visualization, Methodology, Investigation, Formal analysis, Data curation, Conceptualization. **Tiziano Boschetti:** Writing – review & editing, Investigation, Formal analysis, Data curation. **Isabelle Moretti:** Writing – review & editing, Supervision, Conceptualization. **Alessandra Montanini:** Writing – review & editing, Validation, Resources, Investigation, Funding acquisition, Formal analysis, Data curation.

Funding

This study was funded by the Cariparma Foundation (grant 2023–0606).

Declaration of competing interest

The authors declare that they have no known competing financial interests or personal relationships that could have appeared to influence the work reported in this paper.

Acknowledgments

We acknowledge the COMP-R Initiative, funded by the "Departments of Excellence" program of the Italian Ministry for University and Research (MUR, 2023-2027), the Cariparma Foundation (grant 2023-0606) and the Brazilian National Agency of Petroleum, Natural Gas and Biofuels (ANP), for supporting the PhD project of Freitas, V.A. We also acknowledge the contributions of Andrea Artoni, Eleonora Valentini, Moulay Sougrati, Roberto Tinterri, Stefano Segadelli, and Ugo Geymond, whose support was essential to the completion of this study. We sincerely thank the Editor (Marco Fiorentini) and the two anonymous reviewers for their constructive comments and valuable suggestions, which have greatly improved this manuscript.

Appendix A. Supplementary data

Supplementary data to this article can be found online at https://doi.org/10.1016/j.chemgeo.2026.123266.

Data availability

The authors confirm that the data supporting the findings of this study are available within the article and its supplementary materials.

References

Acosta, D.B., Toscani, G., Colombera, L., Amadori, C., Fantoni, R., Di Giulio, A., 2024. Predicting the thermal regime of the Po Plain subsurface (Italy) using geostatistical modeling constrained by legacy wells. Mar. Pet. Geol. 167, 106936. https://doi.org/10.1016/j.marpetgeo.2024.106936.

Allen, D.E., Seyfried Jr., W.E., 2003. Compositional controls on vent fluids from ultramafic-hosted hydrothermal systems at mid-ocean ridges: an experimental study at 400 C, 500 bars. Geochim. Cosmochim. Acta 67 (8), 1531–1542. https://doi.org/10.1016/S0016-7037(02)01173-0.

Artoni, A., Bernini, M., Papani, G., Vescovi, P., Zanzucchi, G., 1992. Sezione geologica schematica Bonassola (SP)-Felino (PR). Studi Geol. Camerti 2, 61–63 (http://193.204.8.201:8080/jspui/handle/1336/413).

Awolayo, A.N., Tutolo, B.M., 2022. PyGeochemCalc: A Python package for geochemical thermodynamic calculations from ambient to deep Earth conditions. Chem. Geol. 606, 120984. https://doi.org/10.1016/j.chemgeo.2022.120984.

Bach, W., Garrido, C.J., Paulick, H., Harvey, J., Rosner, M., 2004. Seawater-peridotite interactions: first insights from ODP Leg 209, MAR 15 N. Geochem. Geophys. Geosyst. 5 (9). https://doi.org/10.1029/2004GC000744.

Balabane, M., Galimov, E., Hermann, M., Letolle, R., 1987. Hydrogen and carbon isotope fractionation during experimental production of bacterial methane. Org. Geochem. 11 (2), 115–119.

Barbieri, M., Boschetti, T., Barberio, M.D., Billi, A., Franchini, S., Iacumin, P., Selmo, E., Petitta, M., 2020. Tracing deep fluid source contribution to groundwater in an active seismic area (central Italy): A combined geothermometric and isotopic ($\delta^{13}C$) perspectiv. J. Hydrol. 582. https://doi.org/10.1016/j.jhydrol.2019.124495.

Barozzi, L., 2019. Il rapporto isotopico $^{13}C/^{12}C$ del carbonio inorganico disciolto (DIC) come tracciante di fluidi profondi. MSc-Thesis (in Italian). University of Parma, Italy.

Bethke, C.M., Farrell, B., Shariki, M., 2025. The Geochemist's Workbench, Version 18.0: GWB Essentials Guide. Aqueous Solutions, LLC, Champaign, Illinois, US.

Binfu, X., Yilong, C., 1999. Mössbauer study of brucite (Mg, Fe)(OH) 2. Wuhan Univ. J. Nat. Sci. 4 (1), 54–56. https://doi.org/10.1007/BF02827620.

Blanc, P., Lassin, A., Piantone, P., Azaroual, M., Jacquemet, N., Fabbri, A., Gaucher, E.C., 2012. Thermoddem: A geochemical database focused on low temperature water/rock interactions and waste materials. Appl. Geochem. 27 (10), 2107–2116. https://doi.org/10.1016/j.apgeochem.2012.06.002.

Blanc, P., Gherardi, F., Vieillard, P., Marty, N.C., Gailhanou, H., Gaboreau, S., Letat, B., Geloni, C., Gaucher, G.C., Madé, B., 2021. Thermodynamics for clay minerals: Calculation tools and application to the case of illite/smectite interstratified minerals. Appl. Geochem. 130, 104986. https://doi.org/10.1016/j.apgeochem.2021.104986.

Boschetti, T., Toscani, L., 2008. Springs and streams of the Taro–Ceno Valleys (Northern Apennine, Italy): reaction path modeling of waters interacting with serpentinized ultramafic rocks. Chem. Geol. 257, 76–91. https://doi.org/10.1016/j.chemgeo.2008.08.017.

Boschetti, T., Etiope, G., Pennisi, M., Romain, M., Toscani, L., 2013. Boron, lithium and methane isotope composition of hyperalkaline waters (Northern Apennines, Italy): terrestrial serpentinization or mixing with brine? Appl. Geochem. 32, 17–25. https://doi.org/10.1016/j.apgeochem.2012.08.018.

Boschetti, T., Cifuentes, J., Iacumin, P., Selmo, E., 2019. Local meteoric water line of Northern Chile (18 S–30 S): an application of error-in-variables regression to the oxygen and hydrogen stable isotope ratio of precipitation. Water 11 (4), 791. https://doi.org/10.3390/w11040791.

Boulart, C., Chavagnac, V., Monnin, C., Delacour, A., Ceuleneer, G., Hoareau, G., 2013. Differences in gas venting from ultramafic-hosted warm springs: the example of Oman and Voltri ophiolites. Ofioliti 38 (2), 143–156. https://doi.org/10.4454/ofioliti.v38i2.423.

Bruni, J., Canepa, M., Chiodini, G., Cioni, R., Cipolli, F., Longinelli, A., Marini, L., Ottonello, G., Zuccolini, M.V., 2002. Irreversible water–rock mass transfer accompanying the generation of the neutral, Mg–HCO3 and high-pH, Ca–OH spring waters of the Genova province, Italy. Appl. Geochem. 17 (4), 455–474. https://doi.org/10.1016/S0883-2927(01)00113-5.

Cao, X., Prozorov, R., Koltypin, Y., Kataby, G., Felner, I., Gedanken, A., 1997. Synthesis of pure amorphous Fe2O3. J. Mater. Res. 12 (2), 402–406. https://doi.org/10.1557/JMR.1997.0058.

Chavagnac, V., Monnin, C., Ceuleneer, G., Boulart, C., Hoareau, G., 2013. Characterization of hyperalkaline fluids produced by low-temperature serpentinization of mantle peridotites in the Oman and Ligurian ophiolites. Geochem. Geophys. Geosyst. 14 (7), 2496–2522. https://doi.org/10.1002/ggge.20147.

Christensen, J.N., Watkins, J.M., Devriendt, L.S., DePaolo, D.J., Conrad, M.E., Voltolini, M., Yang, W., Dong, W., 2021. Isotopic fractionation accompanying CO2 hydroxylation and carbonate precipitation from high pH waters at the Cedars, California, USA. Geochim. Cosmochim. Acta 301, 91–115. https://doi.org/10.1016/j.gca.2021.01.003.

Cipolli, F., Gambardella, B., Marini, L., Ottonello, G., Zuccolini, M.V., 2004. Geochemistry of high-pH waters from serpentinites of the Gruppo di Voltri (Genova, Italy) and reaction path modeling of CO2 sequestration in serpentinite aquifers. Appl. Geochem. 19 (5), 787–802. https://doi.org/10.1016/j.apgeochem.2003.10.007.

Clark, I.D., Fontes, J.C., Fritz, P., 1992. Stable isotope disequilibria in travertine from high pH waters: Laboratory investigations and field observations from Oman. Geochim. Cosmochim. Acta 56 (5), 2041–2050. https://doi.org/10.1016/0016-7037(92)90328-G.

Conti, P., Cornamusini, G., Carmignani, L., 2020. An outline of the geology of the Northern Apennines (Italy), with geological map at 1: 250,000 scale. Ital. J. Geosci. 139 (2), 149–194. https://doi.org/10.3301/IJG.2019.25.

Duchi, V., Venturelli, G., Boccasavia, I., Bonicolini, F., Ferrari, C., Poli, D., 2005. Studio geochimico dei fluidi dell'Appennino Tosco-Emiliano-Romagnolo. Boll. Soc. Geol. Ital. 124 (2), 475–491 (last access 04/11/2025) Available online: https://pubs.geoscienceworld.org/sgi/italianjgeo/article/124/2/475/74931/Studio-geochimico-dei-fluidi-dell-Appennino-Tosco.

Dugamin, E., Truche, L., Donze, F.V., 2019. Natural hydrogen exploration guide. ISRN Geonum-NST 1, 16.

Dyar, M.D., Agresti, D.G., Schaefer, M.W., Grant, C.A., Sklute, E.C., 2006. Mössbauer spectroscopy of earth and planetary materials. Annu. Rev. Earth Planet. Sci. 34 (1), 83–125. https://doi.org/10.1146/annurev.earth.34.031405.125049.

Ellison, E.T., Templeton, A.S., Zeigler, S.D., Mayhew, L.E., Kelemen, P.B., Matter, J.M., Oman Drilling Project Science Party, 2021. Low-temperature hydrogen formation during aqueous alteration of serpentinized peridotite in the Samail ophiolite. J. Geophys. Res. Solid Earth 126 (6), e2021JB021981. https://doi.org/10.1029/2021JB021981.

Etiope, G., 2023. Massive release of natural hydrogen from a geological seep (Chimaera, Turkey): Gas advection as a proxy of subsurface gas migration and pressurised accumulations. Int. J. Hydrog. Energy 48 (25), 9172–9184. https://doi.org/10.1016/j.ijhydene.2022.12.025.

Etiope, G., Whiticar, M.J., 2019. Abiotic methane in continental ultramafic rock systems: Towards a genetic model. Appl. Geochem. 102, 139–152. https://doi.org/10.1016/j.apgeochem.2019.01.012.

Evans, B.W., Kuehner, S.M., Chopelas, A., 2009. Magnetite-free, yellow lizardite serpentinization of olivine websterite, Canyon Mountain complex, NE Oregon. Am. Mineral. 94 (11−12), 1731–1734. https://doi.org/10.2138/am.2009.3301.

Ferrari, E., Montanini, A., Tribuzio, R., 2022. Rifting evolution of the lithospheric subcontinental mantle: New insights from the External Ligurian ophiolites (Northern Apennine, Italy). Lithos 410, 106571. https://doi.org/10.1016/j.lithos.2021.106571.

Freitas, V. A., Montanini, A., Moretti, I., Artoni, A., Segadelli, S., Izerumugaba, J. de la P., Battani, A., & Etiope, G. (2025). Geological and geochemical approach to natural hydrogen exploration in the Northern Apennines, Italy, Mar. Pet. Geol., 182, 107594. doi:https://doi.org/10.1016/j.marpetgeo.2025.107594.

Geymond, U., Briolet, T., Combaudon, V., Sissmann, O., Martinez, I., Duttine, M., Moretti, I., 2023. Reassessing the role of magnetite during natural hydrogen generation. Front. Earth Sci. 11, 1169356. https://doi.org/10.3389/feart.2023.1169356.

Geymond, U., Loiseau, K., Roche, V., Pasquet, G., Revillon, S., Sougrati, M., Moretti, I., 2025. Mössbauer spectroscopy: a key tool to quantify Fe-speciation and distribution in H2-generating rocks. Appl. Geochem. 187, 106399. https://doi.org/10.1016/j.apgeochem.2025.106399.

Goneková, Z., Miglierini, M., Urík, M., Bujdoš, M., Cesnek, M., Kmječ, T., 2020. Identification of magnetic phases in natural ochres by mössbauer spectroscopy. Acta Phys. Pol. A 137, 667. https://doi.org/10.12693/APhysPolA.137.667.

Hart, S.R., Zindler, A., 1986. In search of a bulk-Earth composition. Chem. Geol. 57 (3–4), 247–267. https://doi.org/10.1016/0009-2541(86)90053-7.

Holm, N.G., Oze, C., Mousis, O., Waite, J.H., Guilbert-Lepoutre, A., 2015. Serpentinization and the formation of H2 and CH4 on celestial bodies (planets, moons, comets). Astrobiology 15 (7), 587–600. https://doi.org/10.1089/ast.2014.1188.

Huang, R.F., Sun, W.D., Ding, X., Liu, J.Z., Peng, S.B., 2015. Olivine versus peridotite during serpentinization: Gas formation. Sci. China Earth Sci. 58, 2165–2174. https://doi.org/10.1007/s11430-015-5222-3.

IEA, 2024. Global Hydrogen Review 2024 (last access 23/06/2025). Available online. https://www.iea.org/reports/global-hydrogen-review-2024.

Jagoutz, E., Palme, H., Baddenhausen, H., Blum, K., Cendales, M., Dreibus, G., Spettel, V., Wänke, H., 1979. The abundances of major, minor and trace elements in the earth's mantle as derived from primitive ultramafic nodules. In: Proceedings of the 10th Lunar and Planetary Science Conference, Houston, pp. 2031–2050.

Kelemen, P.B., Leong, J.A., Carlos de Obeso, J., Matter, J.M., Ellison, E.T., Templeton, A., Nothaft, D.B., Eslami, A., Evans, K., Godard, M., Malvoisin, B., Coggon, J.A., Warsi, N.H., Pezard, P., Choe, S., Teagle, D.A.H., Michibayashi, K., Takazawa, E., Sulaimani, Z.A., 2021. Initial results from the Oman Drilling Project Multi-Borehole Observatory: Petrogenesis and ongoing alteration of mantle peridotite in the weathering horizon. J. Geophys. Res. Solid Earth 126, e2021JB022729. https://doi.org/10.1029/2021JB022729.

Klein, F., Bach, W., Jöns, N., McCollom, T., Moskowitz, B., Berquó, T., 2009. Iron partitioning and hydrogen generation during serpentinization of abyssal peridotites from 15 N on the Mid-Atlantic Ridge. Geochim. Cosmochim. Acta 73 (22), 6868–6893.

Klein, F., Bach, W., McCollom, T.M., 2013. Compositional controls on hydrogen generation during serpentinization of ultramafic rocks. Lithos 178, 55–69. https://doi.org/10.1016/j.lithos.2013.03.008.

Klein, F., Tarnas, J.D., Bach, W., 2020. Abiotic sources of molecular hydrogen on Earth. Elements Int. Mag.Mineral. Geochem. Petrol. 16 (1), 19–24. https://doi.org/10.2138/gselements.16.1.19.

Lasagna, S., Zanzucchi, G., Di Dio, G., Martini, A., 2005. Note Illustrative della Carta geologica d'Italia alla scala 1:50.000 F. 199 Parma Sud, Servizio Geologico d'Italia - ISPRA. https://doi.org/10.15161/oar.it/150124.

Lefeuvre, N., Truche, L., Donzé, F.V., Ducoux, M., Barré, G., Fakoury, R.A., Calassou, S., Gaucher, E.C., 2021. Native H2 exploration in the western Pyrenean foothills. Geochem. Geophys. Geosyst. 22 (8). https://doi.org/10.1029/2021GC009917.

Lefeuvre, N., Truche, L., Donzé, F.V., Vandenborre, J., Gaucher, E.C., Magnin, V., 2025. The contribution of mechanoradical reactions to crustal hydrogen generation. Earth Planet. Sci. Lett. 660, 119363. https://doi.org/10.1016/j.epsl.2025.119363.

Leila, M., Lévy, D., Battani, A., Piccardi, L., Šegvić, B., Badurina, L., Pasquet, G., Combaudon, V., Moretti, I., 2021. Origin of continuous hydrogen flux in gas manifestations at the Larderello geothermal field, Central Italy. Chem. Geol. 585, 120564. https://doi.org/10.1016/j.chemgeo.2021.120564.

Lévy, D., Callot, J.P., Moretti, I., Duttine, M., Dubreuil, B., de Parseval, P., Boudouma, O., 2022. Successive phases of serpentinization and carbonation recorded in the Sivas ophiolite (Turkey), from oceanic crust accretion to post-obduction alteration. BSGF Earth Sci. Bull. 193 (1), 12. https://doi.org/10.1051/bsgf/2022015.

Lévy, D., Roche, V., Pasquet, G., Combaudon, V., Geymond, U., Loiseau, K., Moretti, I., 2023. Natural H2 exploration: tools and workflows to characterize a play. Sci. Technol. Energy Transit. 78, 27. https://doi.org/10.2516/stet/2023021.

Lide, D.R. (Ed.), 2004. CRC Handbook of Chemistry and Physics, 85th ed. CRC Press, pp. 4–61.

Loiseau, K., Aubourg, C., Petit, V., Bordes, S., Lefeuvre, N., Thomas, E., Hoareau, G., Moretti, I., 2024. Hydrogen generation and heterogeneity of the serpentinization process at all scales: Turon de Técouère lherzolite case study, Pyrenees (France). Geoenergy 2 (1), geoenergy2023-024. https://doi.org/10.1144/geoenergy2023-024.

Macleod, G., McKeown, C., Hall, A.J., Russell, M.J., 1994. Hydrothermal and oceanic pH conditions of possible relevance to the origin of life. Orig. Life Evol. Biosph. 24 (1), 19–41. https://doi.org/10.1007/BF01582037.

Mangenot, X., Xie, H., Crémière, A., Giunta, T., Lilley, M., Sissmann, O., Orphan, V., Schimmelmann, A., Gaucher, E.C., Girard, J.P., Eiler, J., 2023. 2H-2H clumping in molecular hydrogen method and preliminary results. Chem. Geol. 621, 121278. https://doi.org/10.1016/j.chemgeo.2022.121278.

Marroni, M., Molli, G., Montanini, A., Tribuzio, R., 1998. The association of continental crust rocks with ophiolites (Northern Apennines, Italy): Implications for the continent–ocean transition. Tectonophysics 292 (1–2), 43–66. https://doi.org/10.1016/S0040-1951(98)00060-2.

Marroni, M., Meneghini, F., Pandolfi, L., 2017. A revised subduction inception model to explain the late cretaceous, double-vergent orogen in the precollisional western Tethys: evidence from the Northern Apennines. Tectonics 36, 2227–2249. https://doi.org/10.1002/2017TC004627.

Mayhew, L.E., Ellison, E.T., 2020. A synthesis and meta-analysis of the Fe chemistry of serpentinites and serpentine minerals. Phil. Trans. R. Soc. A 378 (2165), 20180420. https://doi.org/10.1098/rsta.2018.0420.

Mayhew, L.E., Ellison, E.T., McCollom, T.M., Trainor, T.P., Templeton, A.S., 2013. Hydrogen generation from low-temperature water–rock reactions. Nat. Geosci. 6 (6), 478–484. https://doi.org/10.1038/NGEO1825.

McCollom, T.M., Klein, F., Ramba, M., 2022. Hydrogen generation from serpentinization of iron-rich olivine on Mars, icy moons, and other planetary bodies. Icarus 372, 114754. https://doi.org/10.1016/j.icarus.2021.114754.

Milkov, A.V., Etiope, G., 2018. Revised genetic diagrams for natural gases based on a global dataset of> 20,000 samples. Org. Geochem. 125, 109–120. https://doi.org/10.1016/j.orggeochem.2018.09.002.

Montanini, A., Tribuzio, R., 2015. Evolution of recycled crust within the mantle: constraints from the garnet pyroxenites of the External Ligurian ophiolites (northern Apennines, Italy). Geology 43 (10), 911–914. https://doi.org/10.1130/G36877.1.

Montanini, A., Tribuzio, R., Anczkiewicz, R., 2006. Exhumation history of a garnet pyroxenite-bearing mantle section from a continent–ocean transition (Northern

Apennine ophiolites, Italy). J. Petrol. 47 (10), 1943–1971. https://doi.org/10.1093/petrology/egl032.
Montanini, A., Tribuzio, R., Vernia, L., 2008. Petrogenesis of basalts and gabbros from an ancient continent–ocean transition (External Liguride ophiolites, Northern Italy). Lithos 101 (3–4), 453–479. https://doi.org/10.1016/j.lithos.2007.09.007.
Montanini, A., Tribuzio, R., Thirlwall, M., 2012. Garnet clinopyroxenite layers from the mantle sequences of the Northern Apennine ophiolites (Italy): evidence for recycling of crustal material. Earth Planet. Sci. Lett. 351, 171–181. https://doi.org/10.1016/j.epsl.2012.07.033.
Montanini, A., Luguet, A., van Acken, D., Tribuzio, R., Schuth, S., Nowell, G.M., 2025. From crustal protoliths to mantle garnet pyroxenites: insights from Os isotopes and highly siderophile elements. Geochim. Cosmochim. Acta 402, 217–233. https://doi.org/10.1016/j.gca.2025.05.033.
Neubeck, A., Duc, N.T., Bastviken, D., Crill, P., Holm, N.G., 2011. Formation of H 2 and CH 4 by weathering of olivine at temperatures between 30 and 70 C. Geochem. Trans. 12, 1–10. https://doi.org/10.1186/1467-4866-12-6.
Ni, Y., Zhang, J., Yao, L., Dong, G., Wang, Y., Wang, L., Chen, J., 2025. Application of carbon and hydrogen isotopes in the study of natural gas origins. J. Nat. Gas Geosci. 10 (2), 75–85. https://doi.org/10.1016/j.jnggs.2025.02.001.
Pamlć, J., Majer, V., 1977. Ultramafic rocks of the Dinaride central ophiolite zone in Yugoslavia. J. Geol. 85 (5), 553–569. https://doi.org/10.1086/628337.
Parkhurst, D.L., Appelo, C.A.J., 2013. Description of Input and examples for PHREEQC Version 3–a Computer Program for Speciation, Batch-Reaction, One-Dimensional Transport, and Inverse Geochemical Calculations, U.S. Geological Survey Techniques and Methods, Book 6, Chap. A43. U.S.G.S, Reston, VA, p. 497. https://pubs.usgs.gov/tm/06/a43/pdf/tm6-A43.pdf.
Parkhurst, D.L., Charlton, S.R., 2008. NetpathXL – An Excel Interface to the Program NETPATH - U.S. Geological Survey Techniques and Methods 6–A26, Reston, Virginia. https://doi.org/10.3133/tm6A26.
Pasquet, G., Loiseau, K., Diatta, M., Firpo, G., Swire, P., Amey, A., Burckhart, T., Moretti, I., 2025. Natural Hydrogen in the Northern Semail Ophiolite: A Case Study in the Emirate of Ras Al Khaimah, UAE. IJHE. https://doi.org/10.1016/j.ijhydene.2025.02.259.
Piccardo, G.B., Vannucci, R., Guarnieri, L., 2009. Evolution of the lithospheric mantle in an extensional setting: Insights from ophiolitic peridotites. Lithosphere 1 (2), 81–87. https://doi.org/10.1130/L30.1.
Plummer, N., Prestemon, E.C., Parkhurst, D.L., 1994. An interactive code (NETPATH) for modeling NET geochemical reactions along a flow PATH, version 2.0, U.S. Geological Survey; USGS Earth Science Information Center. Open-File Rep. Sect. https://doi.org/10.3133/wri944169.
Portella, Y.M., Conceição, R.V., Siqueira, T.A., Gomes, L.B., Iglesias, R.S., 2024. Experimental evidence of pressure effects on spinel dissolution and peridotite serpentinization kinetics under shallow hydrothermal conditions. Geosci. Front. 15 (2), 101763. https://doi.org/10.1016/j.gsf.2023.101763.
Rancourt, D.G., 1998. Mössbauer spectroscopy in clay science. Hyperfine Interact. 117 (1), 3–38. https://doi.org/10.1023/A:1012651628508.
Rivard, C., Montargès-Pelletier, E., Vantelon, D., Pelletier, M., Karunakaran, C., Michot, L.J., Villieras, F., Michau, N., 2013. Combination of multi-scale and multi-edge X-ray spectroscopy for investigating the products obtained from the interaction between kaolinite and metallic iron in anoxic conditions at 90° C. Phys. Chem. Miner. 40 (2), 115–132. https://doi.org/10.1007/s00269-012-0552-6.
Russell, M.J., Hall, A.J., Martin, W., 2010. Serpentinization as a source of energy at the origin of life. Geobiology 8 (5), 355–371. https://doi.org/10.1111/j.1472-4669.2010.00249.x.
Sanfilippo, A., Tribuzio, R., 2011. Melt transport and deformation history in a nonvolcanic ophiolitic section, northern Apennines, Italy: Implications for crustal accretion at slow spreading settings. Geochem. Geophys. Geosyst. 12, Q0AG04. https://doi.org/10.1029/2010GC003429.
Schwarzenbach, E.M., Vogel, M., Früh-Green, G.L., Boschi, C., 2021. Serpentinization, carbonation and metasomatism of ultramafic sequences in the Northern Apennine ophiolite (NW Italy). J. Geophys. Res. Solid Earth 126, e2020JB020619. https://doi.org/10.1029/2020JB020619.
Segadelli, S., 2014. Funzionamento idrogeologico di acquiferi peridotitici: il caso del M. Prinzera (Appennino settentrionale, Italia). PhD Thesis (in italian). University of Parma.
Segadelli, S., Vescovi, P., Ogata, K., Chelli, A., Zanini, A., Boschetti, T., Petrella, E., Toscani, L., Gargini, A., Celico, F., 2017. A conceptual hydrogeological model of ophiolitic aquifers (serpentinised peridotite): the test example of Mt. Prinzera (Northern Italy). Hydrol. Process. 31 (5), 1058–1073. https://doi.org/10.1002/hyp.11090.
Sougrati, M.T., Jouen, S., Hannoyer, B., Lefez, B., 2008. Hyperfine interactions and lattice dynamics of Sn21O6Cl16(OH)14. J. Solid State Chem. 181, 2473–2479. https://doi.org/10.1016/j.jssc.2008.06.020.
Sougrati, M.T., Goellner, V., Schuppert, A.K., Stievano, L., Jaouen, F., 2016. Probing active sites in iron-based catalysts for oxygen electro-reduction: A temperature-dependent 57 Fe Mössbauer spectroscopy study. Catal. Today 262, 110–120. https://doi.org/10.1016/j.cattod.2015.10.017.
Tribuzio, R., Molli, G., Riccardi, M.P., Messiga, B., 1997. Poliphase metamorphism in ophiolitic gabbros from Bonassola (Internal Liguride units, northern Apennines): A record of western Tethys oceanization. Ofioliti 22, 163–174.
Tutolo, B.M., Tosca, N.J., 2023. Observational constraints on the process and products of Martian serpentinization. Sci. Adv. 9 (5), eadd8472. https://doi.org/10.1126/sciadv.add8472.
Tutolo, B.M., Evans, B.W., Kuehner, S.M., 2019. Serpentine–hisingerite solid solution in altered ferroan peridotite and olivine gabbro. Minerals 9 (1), 47. https://doi.org/10.3390/min9010047.
Tutolo, B.M., Seyfried, W.E., Tosca, N.J., 2020. A seawater throttle on H_2 production in Precambrian serpentinizing systems. Proc. Natl. Acad. Sci. 117 (26), 14756–14763. https://doi.org/10.1073/pnas.1921042117.
Vacquand, C., Deville, E., Beaumont, V., Guyot, F., Sissmann, O., Pillot, D., Arcilla, C., Prinzhofer, A., 2018. Reduced gas seepages in ophiolitic complexes: Evidences for multiple origins of the H2-CH4-N2 gas mixtures. Geochim. Cosmochim. Acta 223, 437–461. https://doi.org/10.1016/j.gca.2017.12.018.
van Dam, F., Kietäväinen, R., Westmeijer, G., Reinhardt, M., Ono, S., Dopson, M., Ketzer, M., McIntosh, J.C., Drake, H., 2025. Microbial methanogenesis fueled by freshwater infiltration and oil biodegradation in the Siljan impact structure, Sweden. Discov. Appl. Sci. 7 (1), 51. https://doi.org/10.1007/s42452-024-06418-8.
Vinson, D.S., Blair, N.E., Martini, A.M., Larter, S., Orem, W.H., McIntosh, J.C., 2017. Microbial methane from in situ biodegradation of coal and shale: A review and reevaluation of hydrogen and carbon isotope signatures. Chem. Geol. 453, 128–145. https://doi.org/10.1016/j.chemgeo.2017.01.027.
Waanders, F.B., 2013. The use of Mössbauer spectroscopy in coal research: is it relevant or not? Mössbauer Spectroscopy 576, 592. https://doi.org/10.1002/9781118714614.ch30.
Wang, J., Watanabe, N., Okamoto, A., Nakamura, K., Komai, T., 2020. Characteristics of hydrogen production with carbon storage by CO2-rich hydrothermal alteration of olivine in the presence of Mg–Al spinel. Int. J. Hydrog. Energy 45 (24), 13163–13175. https://doi.org/10.1016/j.ijhydene.2020.03.032.
Worman, S.L., Pratson, L.F., Karson, J.A., Schlesinger, W.H., 2020. Abiotic hydrogen (H_2) sources and sinks near the Mid-Ocean Ridge (MOR) with implications for the subseafloor biosphere. Proc. Natl. Acad. Sci. 117 (24), 13283–13293. https://doi.org/10.1073/pnas.2002619117.
Zgonnik, V., 2020. The occurrence and geoscience of natural hydrogen: A comprehensive review. Earth Sci. Rev. 203, 103140. https://doi.org/10.1016/j.earscirev.2020.103140.
Zgonnik, V., Beaumont, V., Larin, N., Pillot, D., Deville, E., 2019. Diffused flow of molecular hydrogen through the Western Hajar mountains, Northern Oman. Arab. J. Geosci. 12 (3), 71. https://doi.org/10.1007/s12517-019-4242-2.